


A single-cell atlas of the aging mouse ovary

Received: 12 May 2023

Accepted: 1 December 2023

Published online: 10 January 2024

 Check for updates

José V. V. Isola^{1,8}, Sarah R. Ocañas^{2,3,4,5,8}, Chase R. Hubbart¹, Sunghwan Ko^{2,3}, Samim Ali Mondal¹, Jessica D. Hense^{1,6}, Hannah N. C. Carter⁷, Augusto Schneider⁶, Susan Kovats⁷, José Alberola-Ila⁷, Willard M. Freeman^{2,5} & Michael B. Stout^{1,5} ✉

Ovarian aging leads to diminished fertility, dysregulated endocrine signaling and increased chronic disease burden. These effects begin to emerge long before follicular exhaustion. Female humans experience a sharp decline in fertility around 35 years of age, which corresponds to declines in oocyte quality. Despite a growing body of work, the field lacks a comprehensive cellular map of the transcriptomic changes in the aging mouse ovary to identify early drivers of ovarian decline. To fill this gap we performed single-cell RNA sequencing on ovarian tissue from young (3-month-old) and reproductively aged (9-month-old) mice. Our analysis revealed a doubling of immune cells in the aged ovary, with lymphocyte proportions increasing the most, which was confirmed by flow cytometry. We also found an age-related downregulation of collagenase pathways in stromal fibroblasts, which corresponds to rises in ovarian fibrosis. Follicular cells displayed stress-response, immunogenic and fibrotic signaling pathway inductions with aging. This report provides critical insights into mechanisms responsible for ovarian aging phenotypes. The data can be explored interactively via a Shiny-based web application.

Ovarian aging has garnered substantial attention in recent years due to a large proportion of female humans choosing to delay childbearing¹, which often causes difficulty with conception and carrying a pregnancy to full term². As the ovary ages the local microenvironment changes in ways that reduce oocyte quality and increase the rate of follicular depletion, which eventually results in menopause. Menopause is associated with accelerated systemic aging³, greater chronic disease burden^{4–6} and increased all-cause mortality risk⁷. Therefore, a deeper understanding of the mechanisms that underlie ovarian aging is critically important to extending female fertility and attenuating age-related chronic disease onset.

It is well established that age-related ovarian follicular depletion is associated with increased mitochondrial dysfunction⁸, reactive oxygen species production^{9,10}, inflammation^{11–13} and fibrosis^{14,15}. However, very

little is known about which cell types develop these phenotypes first and/or dominantly contribute to the changing local microenvironment. Moreover, it remains unclear whether cells in the follicle, stroma or both play mechanistic roles in the promotion of follicular depletion and ovarian failure. Recent work has sought to unravel the potential role played by ovarian stromal cells in ovarian health and disease^{12,15,16}. We and others have reported that markers of cellular senescence and fibrogenesis increase within the ovarian stroma with aging^{11,12,15}, although the specific cell types that become senescent and/or profibrotic remain unknown. In addition to increased senescence and fibrotic markers, the ovarian stroma also accumulates multinucleated giant cells (MNGCs) with advancing age, which may be related to the mechanisms that promote the aforementioned phenotypes¹⁷.

¹Aging & Metabolism Research Program, Oklahoma Medical Research Foundation, Oklahoma City, OK, USA. ²Genes & Human Disease Research Program, Oklahoma Medical Research Foundation, Oklahoma City, OK, USA. ³Neuroscience Department, University of Oklahoma Health Sciences Center, Oklahoma City, OK, USA. ⁴Physiology Department, University of Oklahoma Health Sciences Center, Oklahoma City, OK, USA. ⁵Oklahoma City Veterans Affairs Medical Center, Oklahoma City, OK, USA. ⁶Nutrition College, Federal University of Pelotas, Pelotas, Brazil. ⁷Arthritis & Clinical Immunology Research Program, Oklahoma Medical Research Foundation, Oklahoma City, OK, USA. ⁸These authors contributed equally: José V. V. Isola, Sarah R. Ocañas. ✉e-mail: michael-stout@omrf.org

Due to the complex nature of ovarian function, which changes dynamically during aging, it has historically been challenging to elucidate the cell type-specific mechanisms that promote follicular depletion and ovarian failure. Data showing age-related changes in ovarian transcriptional programs within cellular subtypes are limited, particularly those pertaining to mice. Single-cell analyses of ovarian aging in nonhuman primates identified downregulation of antioxidant programs in aged oocytes and increased apoptosis in aged granulosa cells (GCs)¹⁸. In addition, single-cell analyses of human ovarian tissue are currently in progress¹⁹. However, mice represent the model organism most utilized for ovarian aging studies²⁰ due to their short lifespan and ease of genetic manipulation for mechanistic studies. One spatially resolved analysis of mouse ovaries made strides in identifying age-related changes in ovarian cell populations²¹. However, this study used reproductively senescent (15-month-old) mice and lacked the resolution to identify specific cellular subtypes and important immune populations. To add to this growing body of work, we performed single-cell RNA sequencing (scRNA-seq) to identify age-related transcriptional changes in a cell type-specific manner within the mouse ovary at 3 and 9 months of age. We chose to analyze 3- and 9-month-old mice because they remain reproductively active at both ages, yet this age interlude represents a period when follicular density decreases markedly in conjunction with the emergence of age-related hallmarks¹¹. This design and approach allowed us to determine how aging modulates cellularity and cellular phenotypes within the ovary before reproductive senescence, which is vital to the development of pharmacological approaches for extending the reproductive lifespan in female humans.

Results

scRNA-seq of the adult mouse ovary across reproductive ages

For evaluation of age-related changes in the ovary we collected ovaries from 3- and 9-month-old female mice ($n = 4$ per group) and performed scRNA-seq. The period from 3 to 9 months represents the time when the greatest decline in follicular reserve occurs and other hallmarks of aging begin to emerge¹¹. Following quality control analyses, filtering and doublet removal, 14,504 cells remained for characterization. Cellular distributions of the number of genes detected, number of molecules and proportion of mitochondrial DNA before and after filtering are shown in Supplementary Fig. 1a. A mitochondrial DNA filtering parameter of 25% was used to ensure the inclusion of oocytes, because these are known to have more mitochondria than somatic cells^{22,23}. In addition, mitochondrial-dependent apoptosis is involved in follicular atresia²⁴ and thus a lower filtering threshold may result in loss of oocytes and follicular cells. Indeed, these clusters (CLUs) showed the highest mtDNA percentages among all identified CLUs (Supplementary Fig. 1b). Unbiased clustering and uniform manifold approximation and projection (UMAP) analysis revealed 15 distinct cellular CLUs (Fig. 1a). One CLU was present in only one sample and was subsequently identified as oviduct contamination (Supplementary Fig. 1c) and therefore these cells were removed from further analyses, which left 14,349 cells for downstream analyses. To assign cell type identity we used cell type-specific markers previously reported in the literature.

Collectively, the most common cell type was found to be stromal cells ($n = 5,671$), which segregated into three CLUs. One stromal CLU, referred to as Stroma A, was characterized by having a major *Col1a1* transcriptional signature²⁵ as well as other stromal markers. A second CLU, Stroma B, was identified by the expression of several stromal markers (*Bgn*, *Ogn*, *Dcn*, *Lum*, *Col1a1* (ref. 26)). However, this CLU did not have any exclusive markers that were highly enriched. A third stromal CLU, Stroma C, was characterized by *Notch3* expression (Fig. 1b), which is classically viewed as a pericyte marker^{26,27}. The second most common cell type was found to be GCs ($n = 3,334$), which segregated into two distinct CLUs, both displaying high expression of *Amh*^{18,28} (Fig. 1b). Other CLUs were identified as theca cells (TCs; $n = 1,637$; *Srd5a1* (ref. 29)), phagocytes (two distinct CLUs; $n = 1,099$; *C1qa* (ref. 30)),

endothelial cells ($n = 798$; *Cd34* (ref. 31)), T lymphocytes ($n = 728$; *Cd3g* (ref. 32)), epithelial cells (two distinct CLUs; $n = 450$; *Upk1b* (ref. 33) or *Gpm6a* (ref. 26)), oocytes ($n = 224$; *Zp3* (ref. 18)), luteal cells ($n = 206$; *Ptgr3*³⁴) and B lymphocytes ($n = 202$; *Cd79a* (ref. 35)) (Fig. 1b). Feature plots showing the specificity of these markers to each CLU can be found in Supplementary Fig. 1d. All markers for each CLU are listed in Supplementary Data 1.

Advancing age changed ovarian cellularity in our analyses (Fig. 2a,b and Supplementary Fig. 1e). The percentage of GCs was lower in 9-month-old ovaries, which can be explained by both declines in the number of primordial and tertiary follicles and a trending decline in secondary follicles observed in the aged mice (Fig. 2c–e). The most marked change in ovarian cellularity with advancing age was the greater than twofold increase in immune cells (Fig. 2a,b and Supplementary Fig. 1e).

In this study, although estrous cycle staging was not performed we used a bioinformatic approach to determine the estrous cycle stage of each mouse at the time of euthanasia. To do this we initially integrated our data with single-cell transcriptomic data from estrous cycle-staged mice²⁶. That report showed major differences in single-cell transcriptional outcomes within GCs across estrous cycle stages, with unique features being observed during both proestrus and estrus. Following integration we then generated UMAP plots of GCs from mice in each estrous cycle stage and observed unique CLUs during both estrus and proestrus, which recapitulated the findings from Morris et al.²⁶. We then created UMAP plots of GCs from each biological replicate in our study to determine whether they were in proestrus or estrus, which could potentially confound the interpretation of age-related transcriptional phenotypes (Supplementary Fig. 2a–d). We found that all four young mice, and three of the old mice, were in either diestrus or metestrus, which are transcriptionally indistinguishable²⁶. One old mouse, Sample 5, was found to be in proestrus. We then used the list of transcripts, as reported by Morris et al.²⁶ (Supplementary Data 1) to be upregulated during proestrus within GCs, to generate a module score for each sample, which enabled us to confirm that Sample 5 was in proestrus. These data are presented in violin plots in Supplementary Fig. 2e. We also performed principal component analysis of differentially expressed genes with age in our samples and observed that the only distinguishable clustering was that according to age (Supplementary Fig. 2f). Assessment of the potential impact of the proestrus sample on age-related phenotypic changes in GCs is discussed later in the manuscript following subcluster (SCL) analyses, although no major changes were observed.

For evaluation of intercellular signaling networks, CellChat analyses were performed. The most notable changes in cell signaling occurred among granulosa, stroma A and epithelium CLUs, with an overall increase in the number of interactions (Supplementary Fig. 3a) and interaction weights (Supplementary Fig. 3b) from 3 to 9 months of age. However, there was not a complete breakdown in cell-to-cell communication with aging.

Ovarian immune cell changes with aging

Following observation of the increased proportion of immune cells within the aged ovary, we performed subclustering of immune cells to determine which specific populations were changed with aging (Fig. 3a). Following reclustering, the original immune cell CLUs separated into 13 SCLs (Fig. 3b). Cell type identification for each SCL was performed based on known gene expression profiles and, with the help of databases Cellmarker2.0 (ref. 36) and ImmGen³⁷, with the representative genes described in Fig. 3c. All markers for immune SCLs are listed in Supplementary Data 1. Because the overall immune cell proportion doubled from 3 to 9 months of age, percentages of total cells in each SCL were assessed and compared by age. Intriguingly, cell types showing the greatest increase with age were lymphoid, including B cells, conventional T cells and innate-like T cells. The biggest difference in

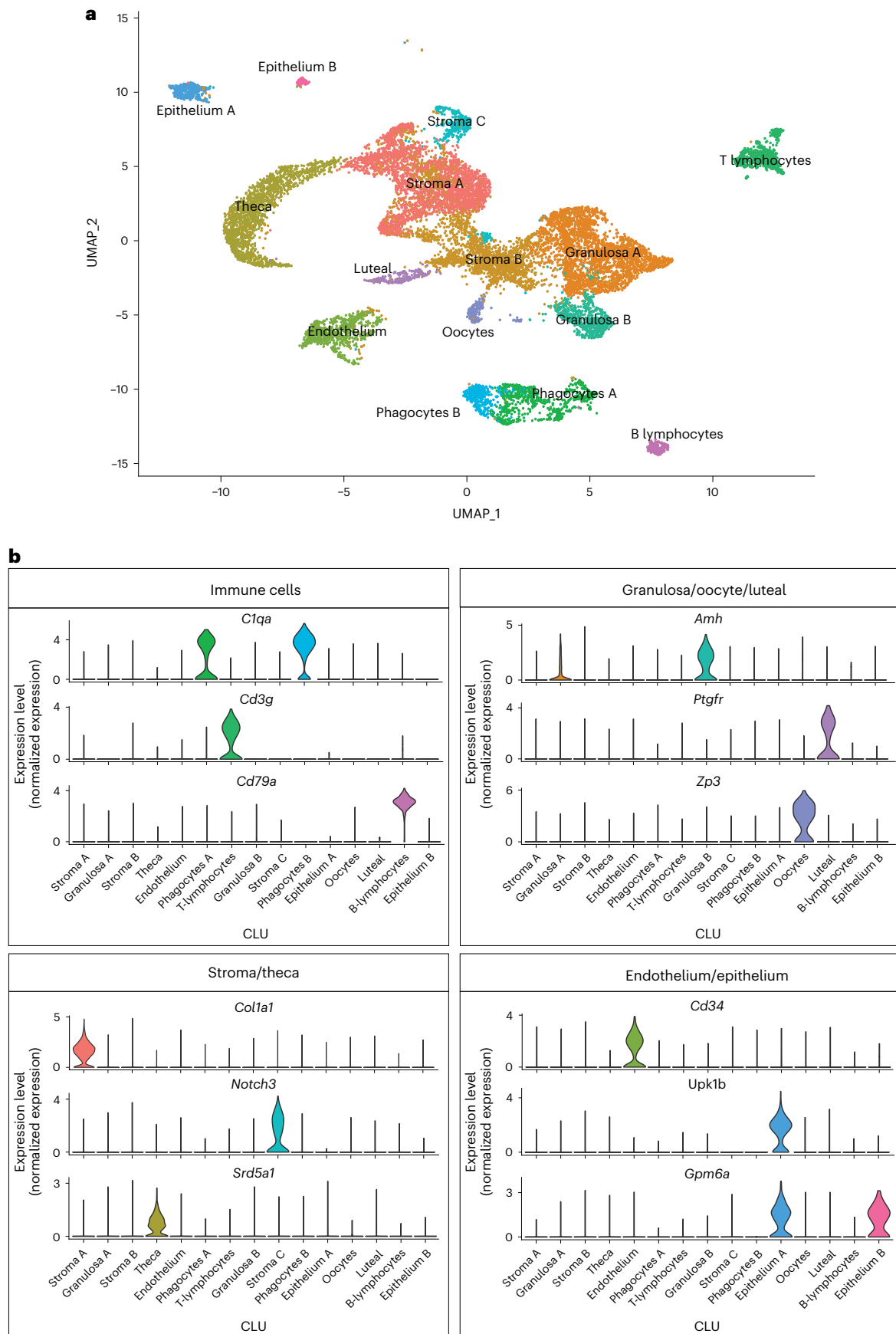


Fig. 1 | scRNA-seq of the mouse ovary. **a**, Whole-ovarian tissue was collected from 3- and 9-month-old C57BL/6 J mice and processed for 10X Genomics 3' scRNA-seq. **a**, UMAP plot of age-combined ovarian cells. Clustering analysis

revealed 15 distinct ovarian cell populations. **b**, Violin plots of specific marker genes for each ovarian cell type. scRNA-seq was performed in $n = 4$ ovaries per age group.

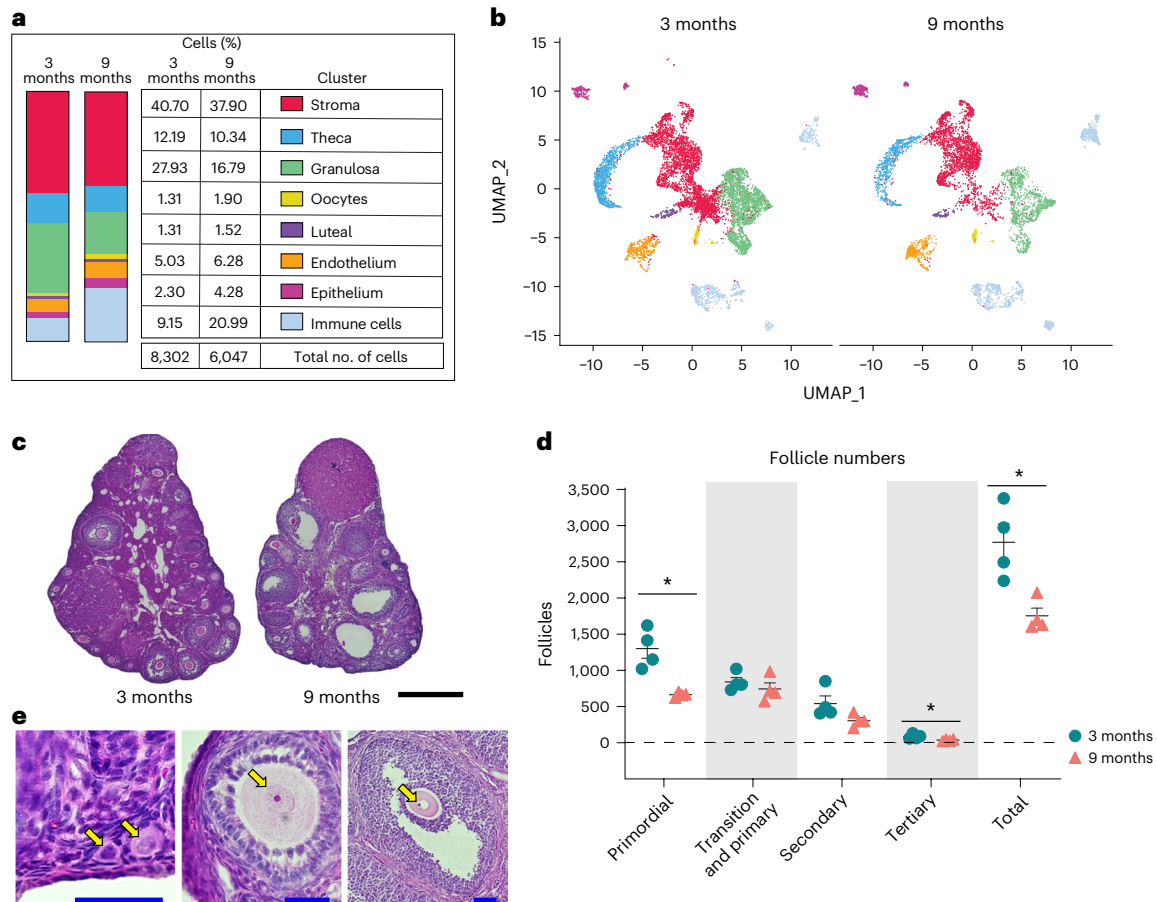


Fig. 2 | Age-related changes in ovarian cell populations. a, Numbers and percentages of cells in broad categories of cell type identity, by age. **b**, UMAP plot of ovarian cells, by age (color coding as in **a**). **c**, Representative images of H&E-stained ovaries. H&E staining and follicle counting were repeated for each biological replicate. Scale bar, 500 μm . **d**, Estimated numbers of follicles in 3- and 9-month-old ovaries. **e**, Representative images of follicles stained by H&E. Arrows

(from left to right) indicate primordial, primary, secondary and tertiary follicles, respectively. Scale bars, 50 μm . Data presented as mean \pm s.e.m. *FDR < 0.05, **FDR = 0.01, ***FDR = 0.005 by multiple two-tailed *t*-test with Benjamini, Krieger and Yekutieli correction for multiple comparisons. scRNA-seq was performed in $n = 4$ ovaries per age group. Exact *P* values shown in Source Data.

abundance with age was in a SCL containing Type 1 lymphoid cells, as defined by the expression of *Tbx21* (ref. 38) and *Irfng*. These probably include CD8⁺ T cells, as well as other Type 1 innate-like T cells such as natural killer T cells (NKT cells), mucosal-associated invariant T cells (MAIT cells) and/or $\gamma\delta$ T cells ($\gamma\delta$ T cells). Another SCL that significantly increased with age contained Type 17 lymphoid cells, as defined by the expression of *Rorc*³⁹, which commonly represents innate lineage and expression of *Zbtb16* (refs. 40,41). Although transcriptional data cannot further discriminate within this SCL, it probably includes Type 17 NKT cells, MAIT cells, $\gamma\delta$ T cells and/or innate lymphoid cells Type 3 (ILC3), which was later confirmed by flow cytometry. Finally, the percentage of CD4⁺ T cells was also increased within the aged ovary (Fig. 3d). It should be noted that, due to single-cell transcriptomic limitations, other conventional T cells may also be contained within the CD4⁺ SCL. Conversely, neither natural killer (NK) cells nor ILC2s were significantly changed with age. Tissue macrophages and monocytes trended towards an increased proportion in the aged ovary but failed to reach statistical significance (Fig. 3d). One SCL, which was present only in the aged ovaries, was identified as monocytes that express CD300e, which negatively regulates T cell activation⁴². These CD300e⁺ monocytes may thus represent a compensatory mechanism to address T cell accumulation. However, this SCL might also represent blood monocyte contamination due to incomplete perfusion. Further investigation into this unique cellular population is warranted. Interestingly, although having an immune-like expression profile, two of the immune SCLs showed no expression of *Ptprc*, the gene that codes for CD45—the most

well-established immune cell marker. These two SCLs were identified as CD45[−] immune-like cells A and B.

To confirm our transcriptional findings related to ovarian immune cell accumulation, we performed high-dimensional flow cytometry to identify age-related differences in the fraction of distinct immune cell types within the ovary. We first assessed the percentage and total number of broadly defined immune cell types, including B cells (CD19⁺), T cells and innate lymphoid cells (CD90⁺) and myeloid cells (CD11b⁺). We observed a higher percentage and number of CD90⁺ cells (T cells and innate lymphoid cells) in aged ovaries (Fig. 3e,f and Supplementary Fig. 4a), which aligns with the scRNA-seq findings. However, we did not observe changes in the percentage or number of myeloid cells or B cells (Fig. 3e,f and Supplementary Fig. 4a). Although the absence of change in myeloid cells was consistent with the scRNA-seq data, the B cells were incongruent. The proportion of B cells was found to increase with aging by scRNA-seq analyses, although this was not confirmed by flow cytometry. UMAP visualization of the flow cytometry data showed major shifts in immune cell subpopulations within the aging ovary (Fig. 4a). We then further characterized the CD90⁺ population and observed an increase in the percentage of CD8⁺ T cells, 'double-negative $\alpha\beta$ T cells' (DNs), MAIT cells, NKT cells and $\gamma\delta$ Ts and a decrease in CD4⁺ $\alpha\beta$ T cells and innate lymphoid cells in aged ovaries (Fig. 4b and Supplementary Fig. 4b). To compare and contrast these findings with scRNA-seq clustering, we analyzed CD90⁺ cells based on expression of the effector-type-determining transcription factors for Type 17 lymphoid cells (ROR γ T) and Type 1 cells (T-BET) (Supplementary

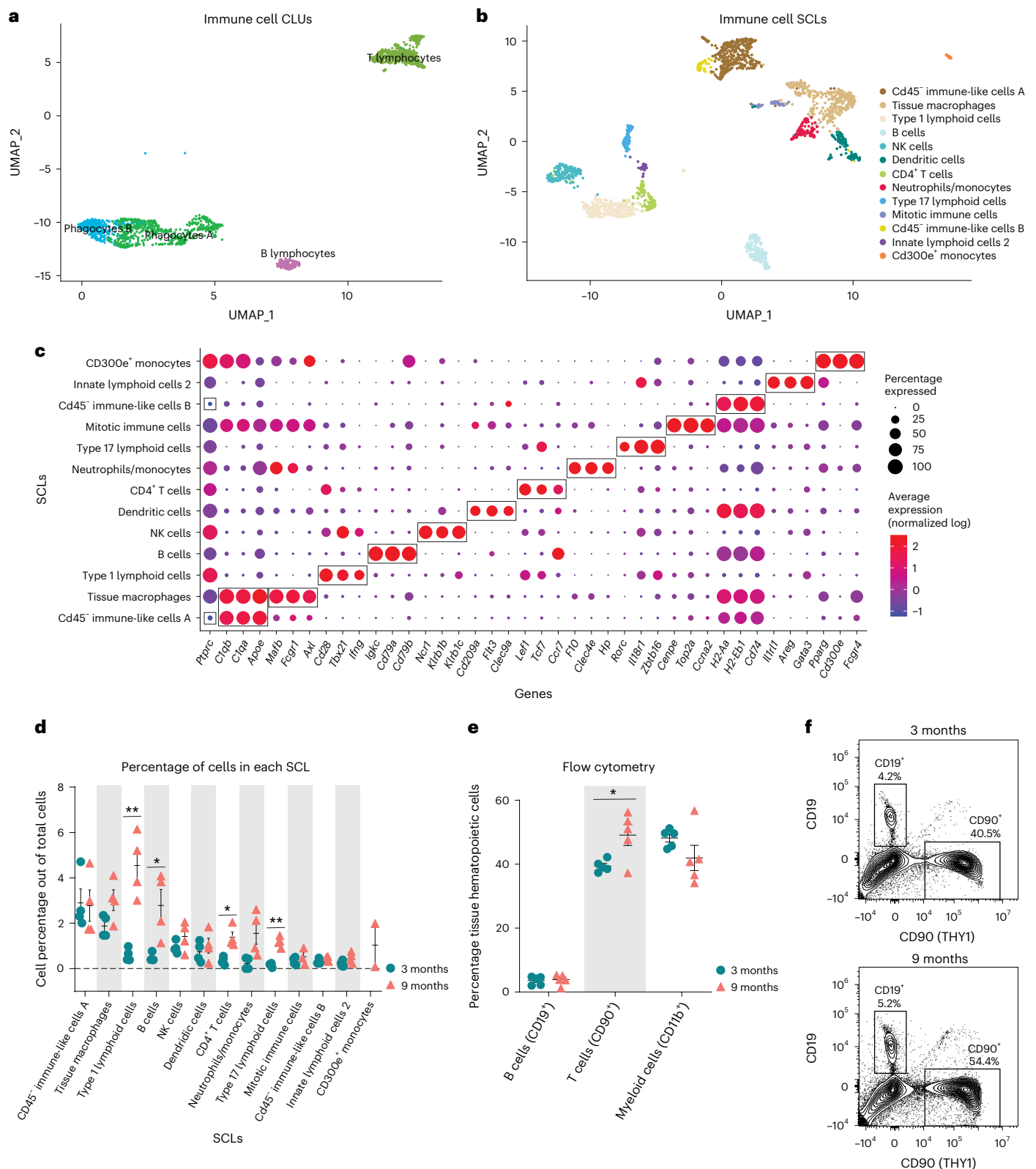


Fig. 3 | Immune cells accumulate in the ovary with age. a, UMAP of immune CLUs selected for subclustering analyses. **b**, UMAP of immune SCLs. **c**, Dot plot of markers used for SCL cell type identification. **d**, Percentages of cells in each immune SCL out of total cells. **e**, Percentages of immune cells out of tissue hematopoietic cells (following gating out of intravascular hematopoietic cells) by flow cytometry. **f**, Representative gating of CD19⁺ and CD90⁺ cells following gating out of tissue hematopoietic cells (intravascular CD45⁺, CD45⁻) in young

and aged ovaries (see Supplementary Fig. 4a for complete gating strategy). For flow cytometry, six ovaries from mice in the same phase of estrous cycle were pooled ($n = 5$ per age group). scRNA-seq was performed in $n = 4$ ovaries per age group. Data presented as mean \pm s.e.m. * $FDR < 0.05$, ** $FDR = 0.01$, *** $FDR = 0.005$ by multiple two-tailed t -test with Benjamini, Krieger and Yekutieli correction for multiple comparisons. Exact P values given in Source Data. THY1, Thy-1 cell surface antigen.

Fig. 4c). The increase in Type 1 lymphoid cells observed with scRNA-seq was confirmed by flow cytometry and further determined that the increase was driven by Type 1 NKT cells, while the proportions of Type 1 DN and $\gamma\delta$ T decreased with age (Fig. 4c,d). All ROR γ T subpopulations increased in proportion with age (DN, NKT, $\gamma\delta$ T) although the greatest magnitude of change occurred in Type 17 $\gamma\delta$ Ts (Fig. 4c,d). Although the scRNA-seq data suggested the presence of ILC2—but not ILC1—subpopulations, the flow cytometry data identified both ILC1s (T-BET⁺) and ILC2s (GATA3^{hi}). The flow cytometry data indicated a decrease in ILC1 percentages with advancing age (Fig. 4e,f). To determine the potential impact of estrous cycle stage on age-related changes in ovarian immune cell populations, we performed vaginal cytology on mice before euthanasia and ovarian flow cytometry analyses. We then plotted the mean fluorescence intensity of all markers assessed in each ovarian sample, in addition to identifying the estrous cycle stage of mice. We found that samples clustered by age, regardless of estrous cycle stage (Supplementary Fig. 4d), thereby indicating that estrous cycle stage is not a primary contributor to age-related changes in immune cell accumulation.

In addition to an overall increase in immune cells within the aged ovary, previous reports have also noted the accumulation of MNGCs as a hallmark of ovarian aging^{17,43}. Although MNGCs were certainly removed from our single-cell suspensions during filtration, we were able to observe them in 9-month-old ovaries via histological assessment. Similar to previous reports^{11,17,44}, we observed MNGCs in the aged ovary (Supplementary Fig. 5a), their presence corresponding to a rise in lipofuscin positivity (Supplementary Fig. 5b), which has been reported to be a marker of cellular senescence⁴⁵. However, it should be noted that lipofuscin positivity strongly associates with increased numbers and size of MNGCs, which may not actually be cellular senescence as classically defined. Given the increased number of immune cells in the aged ovary that inherently express senescence-related genes (Supplementary Fig. 6a,b), it appears likely that ‘ovarian cellular senescence’ before estropause may represent increased immune cell accumulation. However, it should be noted that *Cdkn1a* and *Cdkn2d* expression increased in Type 17 lymphoid cells (Supplementary Fig. 6b–d) with advancing age, which could potentially represent a small subpopulation of cells that enter cellular senescence in the ovary.

Subclustering of stroma and TCs reveals age-related changes

Several changes in the stroma have been observed with ovarian aging and are apparent before follicular exhaustion, including cellular senescence signatures¹¹ and collagen deposition^{12,14,15}. To identify potential cellular and molecular mediators of these phenotypes we performed subclustering of the stroma and TC CLUs (Fig. 5a,b). TCs were included with stroma because they dynamically differentiate from fibroblastic stromal cells during follicular maturation and thus share similarities with stromal cells³⁶. This subclustering resulted in six distinct SCLs (Fig. 5b). Enriched markers in each SCL were used to infer cell type specificity (Fig. 5c). Notably, there was a SCL that expressed *Inhba*^{37,38}, a marker of GCs, that was distinct and thus easily separated from other stroma and TC SCLs. The smooth muscle SCL was identified by the expression of *Myh11* (refs. 46,47), *Actg2* (ref. 26) and *Cnn1* (ref. 48). The pericyte SCL was enriched for *Notch3*, *Rgs5* and *Ebf1* (ref. 26). The fibroblast-like SCL had enrichment of *Dcn*, *Mgp*⁴⁰ and *Lum*²⁶ whereas the TC SCL showed high expression of steroidogenic genes (*Cyp11a1*, *Cyp17a1* (ref. 36) and *Mgarp*²⁶). The early TC SCL also showed high levels

of steroidogenic genes including *Ptch1* and *Hhip*⁴¹, in addition to high expression of a fibroblast gene (*Enpp2* (ref. 42)), suggesting that these cells are in transition from stromal fibroblast-like cells to TCs. All markers for each stromal SCL are listed in Supplementary Data 1.

Following SCL identification, a list of genes differentially expressed by the different ages in each SCL was imported into the software Ingenuity Pathway Analysis (IPA) to infer biological function. Fibroblast-like stromal cells showed an age-related upregulation of pathways related to tissue remodeling^{49,50} (Fig. 5d). Tissue remodeling occurs following ovulation and in cases of follicular and luteal atresia¹⁶. To our surprise, collagen expression was unchanged by aging in ovarian fibroblast-like SCL (Fig. 6a) despite greater collagen deposition by 9 months of age (Fig. 6b). Interestingly, the collagenase pathway was downregulated in the fibroblast-like SCL (Fig. 6c). Further analyses revealed that the expression of matrix metalloproteinase 2 (*Mmp2*), a key enzyme involved in collagen degradation⁵¹, was decreased in the fibroblast-like SCL with advancing age (Fig. 6d). We also observed an age-related decrease in MMP2 protein in the ovarian stroma by immunofluorescence (Fig. 6e,f). These findings suggest that ovarian collagen accumulation is at least partially mediated by a reduction in collagen degradation, which supports our transcriptional findings. Fibroblast-like cells also showed downregulation in hormonal signaling (estrogen receptor and gonadotropin-releasing hormone; Fig. 5d), which is somewhat surprising given that hormone levels, estrous cyclicity and fertility are generally stable at 9 months of age⁵². These results indicate that changes in the local microenvironment may contribute to endocrine dysfunction in the ovarian stroma independently of changes within the follicle. However, fibroblast-like cells showed a downregulation in upstream regulators associated with inflammation and fibrosis (Fig. 6c), which could be a compensatory response to increases in proinflammatory and profibrotic signaling from other cell types, as well as immune cell accumulation. In other tissues, fibroblasts are known to play immunosuppressive roles in the regulation of chronic inflammation⁵³. In contrast to fibroblast-like cells, TCs showed a significant upregulation in several upstream regulators of fibrogenesis including TGF β 1, TGF β 2 and SMAD3 (Fig. 6c), which suggests that TCs may be one of the earliest cell types involved in generation of the signaling cascade for collagen production and deposition.

In contrast to fibroblast-like cells, TCs showed significant upregulation in several upstream regulators of fibrogenesis including TGF β 1, TGF β 2 and SMAD3 (Fig. 6c), which suggests that these may be one of the earliest cell types involved in generating the signaling cascade for collagen production and deposition. When looking at TGF β intercellular communication among the original CLUs, we note that TCs signal to several cell types in the young ovary (Fig. 6g), which was expected, due to its important role in intrafollicular cell-to-cell communication⁵⁴. In contrast, TGF β signaling in TCs from aged ovaries became exclusive to immune cells (Fig. 6h). TGF β signaling has previously been associated with the regulation of chemotaxis, activation and survival of lymphocytes^{55,56}, which may explain our finding of increased lymphocyte accumulation in the aged ovary. Additionally, the Granulosa B CLU showed only TGF β signaling in the old ovary (Fig. 6g,h). These data suggest that interactions between ovarian follicular cells and immune cells are probably important for perpetuation of fibrotic signaling with aging. TCs also showed a modest age-related upregulation in inflammation and cell stress-response pathways (Fig. 6i), which were mirrored by upstream regulators involved in cellular proliferation including MTOR, YAP1 and RB1 (Fig. 6j).

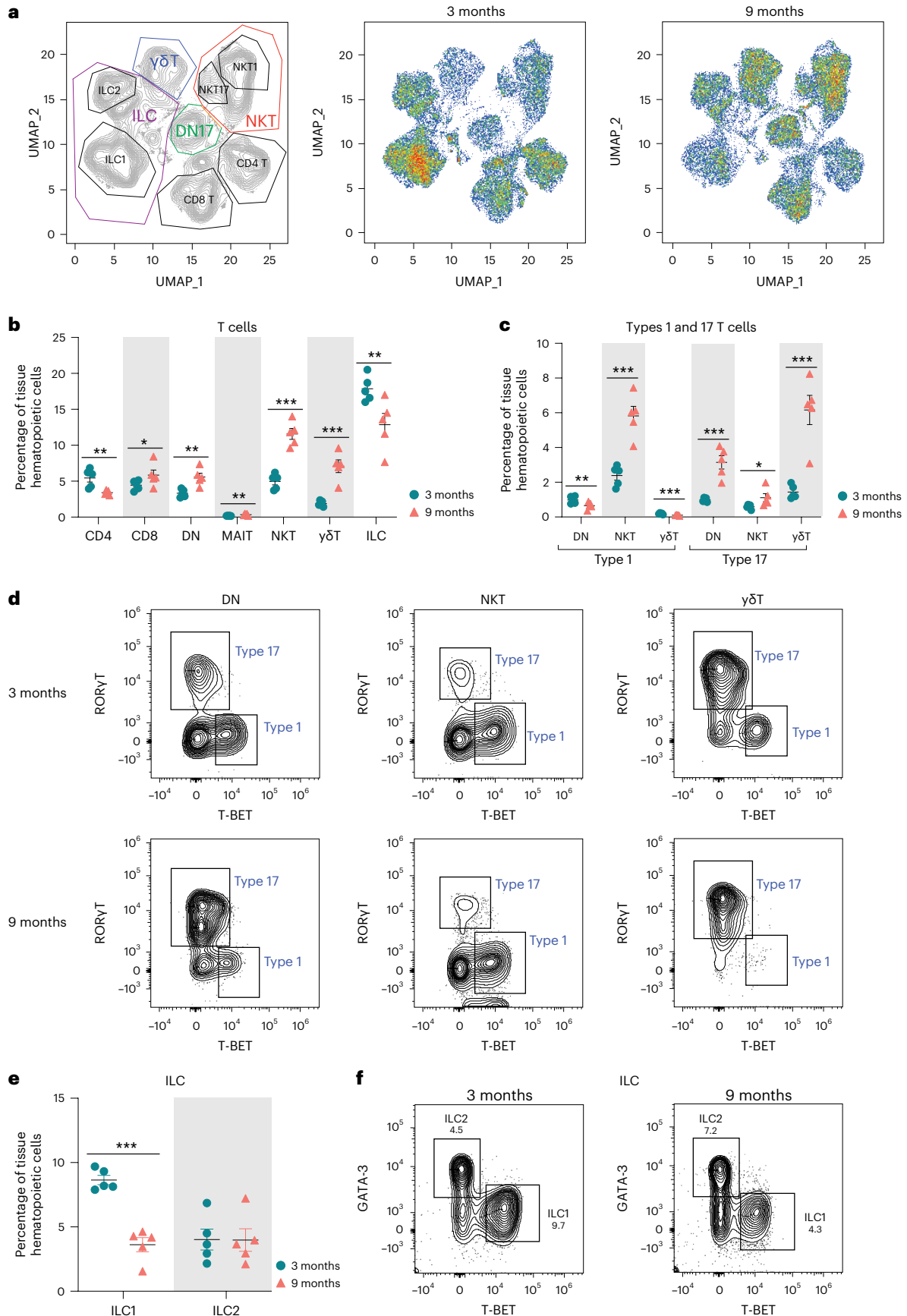
Fig. 4 | Lymphocyte populations are altered in the aged ovary. **a**, UMAP of flow cytometry panel of lymphoid cells, annotated using conventional gating strategies. The number of cells plotted was normalized to better observe differences in population distribution. **b**, Percentage of T cell subpopulations out of tissue hematopoietic cells. **c**, Percentage of Types 1 and 17 T cells out of tissue hematopoietic cells. **d**, Representative gating of Types 1 and 17 lymphoid cells in young and aged ovaries. **e**, Percentages of ICL1 and ILC2 out of tissue

hematopoietic cells. **f**, Representative gating of innate lymphoid cells in young and aged ovaries. For flow cytometry, six ovaries from mice in the estrous cycle stage were pooled ($n = 5$ per age group). Data presented as mean \pm s.e.m. *FDR < 0.05, **FDR = 0.01, ***FDR = 0.005 by multiple two-tailed t -test with Benjamini, Krieger and Yekutieli correction for multiple comparisons. Exact P values are given in Source Data.

Aging affects granulosa, oocyte and luteal cell SCLs

Cellular populations of GCs, oocytes and luteal cells were subclustered into six distinct SCLs (Fig. 7a-c). GCs were further segregated into

four distinct SCLs that were identified as being part of follicles at different stages of development. These SCLs included preantral, antral, mitotic and atretic GCs. GCs signal to oocytes to provide cues



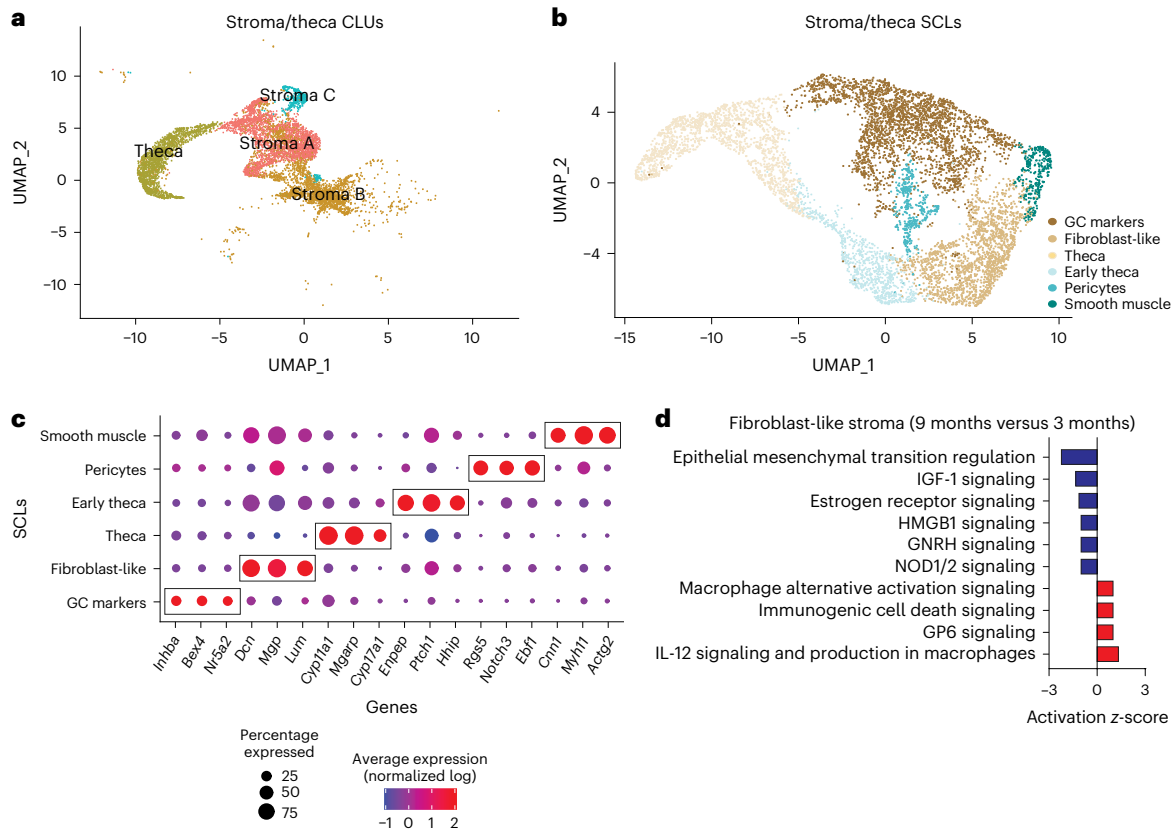


Fig. 5 | Subclustering of stroma and TCs. a, UMAP of stroma and TC CLUs used for subclustering. **b**, UMAP of stroma and TC SCLs. **c**, Dot plot of markers used for SCL cell type identification. **d**, IPA canonical pathways indicating activation or inhibition of specific pathways by aging in stromal fibroblast-like cells. scRNA-seq was performed in $n = 4$ ovaries per age group.

related to the local ovarian microenvironment, in addition to conversion of androgens to estrogens, which are released into the systemic circulation for feedback signaling in the brain⁵⁷. GCs from immature follicles that have not yet developed an antrum are referred to as preantral GCs and were identified by enrichment in *Igfbp5* (ref. 58) and *Gatm*⁵⁹ expression. GCs from antral follicles (antral GCs) were identified by enrichment of *Inhbb*^{60,61}. A separate GC SCL, which we refer to as mitotic GCs, expressed *Inhbb* similarly to antral GCs but showed enriched expression of cell division markers *Top2a* (ref. 62) and *Racgap1* (ref. 63). Last, GCs from follicles undergoing atresia were found to be enriched for *Pik3ip1* (refs. 26,64), *Itih5* (ref. 26) and *Ghr*²⁶. Oocytes were readily identified by the expression of classical markers *Gdf9*, *Ooep* and *Zp3* (ref. 18). Luteal cells, which consist of remnant GCs and TCs following ovulation and constitute the corpus luteum⁶⁵, were identified by the expression of *Ptgr1*³⁴. All markers for each GC SCL can be found in Supplementary Data 1.

As alluded to above, differentially expressed genes from each SCL were examined with IPA software to infer biological function. Interestingly, preantral, antral and atretic GCs all displayed an age-related increase in pathways related to proinflammatory stress and fibrogenesis (Fig. 7d–f). These observations corresponded to a significant increase in the mitochondrial dysfunction pathway within oocytes (Fig. 7g). Upstream regulators related to proinflammatory stress that were found to be increased in GC SCL included IFNG, TNF, IL15 and IL1A (Supplementary Fig. 7a). Additionally, upstream regulators related to fibrogenesis were found to be increased in GC SCL including TGFBI, TGF-beta and SMAD3 (Supplementary Fig. 7a). As expected, the atretic GC SCL was enriched for changes in proinflammatory stress and fibrosis pathways, with 9-month-old mice having greater activation of these pathways than 3-month-old mice. Therefore, it appears that aging exacerbates inflammatory and fibrotic responses that are required for ovarian remodeling following ovulation and follicular atresia.

We also examined intercellular C–C motif chemokine ligand (CCL) signaling due to its role in immune cell migration and chemotaxis. We found that, by 9 months of age, granulosa CLUs expressed CCL signaling molecules, which was not observed in 3-month-old mice (Supplementary Fig. 7b,c). At 9 months of age GC CCL signaling was exclusive to the phagocyte A CLU. This suggests that inflammatory signaling from the follicle may contribute to alterations in immune cell phenotypes as a function of age. Interestingly, there was a breakdown in the anti-Müllerian hormone signaling pathway between oocytes and other follicular cells by 9 months of age (Supplementary Fig. 7d,e). The anti-Müllerian hormone pathway is critical for regulation of follicular maturation⁶⁶ and is commonly used as a marker of follicular reserve⁶⁷. This breakdown in signaling therefore signifies early changes that may impact reproductive outcomes.

Because GC transcriptional changes have been reported during proestrus, coupled with one of the 9-month-old mice (Sample 5) analyzed herein being in proestrus, we performed additional analyses to ensure that estrous cycle stage did not confound our age-related interpretations. For this analysis we removed those genes that were found to be differentially expressed in both proestrus²⁶ and aging in granulosa SCLs, and reran the pathway analyses. The removal of these genes did not affect age-related changes in GCs. As a secondary confirmation we then completely removed Sample 5, reran the pathway analysis and found that age-related outcomes were unchanged (Supplementary Fig. 7f). These observations provide additional evidence that our interpretations related to the mechanisms promoting ovarian aging are unaffected by estrous cycle stage.

Endothelial and epithelial SCLs are mildly affected by age

Endothelial cells are essential components of blood and lymphatic vessels. The ovary is a highly vascularized organ with blood vessels that travel through connective tissue to assist with hormone/nutrient

trafficking and waste removal⁶⁸. The ovary also has a rich lymphatic network, closely associated with the blood vasculature, that is involved in immune cell trafficking⁶⁹. Epithelial cells comprise the ovarian surface, facilitate repair following ovulation and dynamically expand and contract during cyclic ovarian changes⁷⁰. In addition, epithelial cells share a common progenitor with GCs⁷¹. Endothelial and epithelial CLUs were subclustered (Fig. 8a), resulting in four distinct SCLs (Fig. 8b). Vascular and lymphatic endothelia were separated and identified by the enrichment of specific cellular markers (Fig. 8c). Vascular endothelial cells showed enrichment of *Flt1* (ref. 72) and *Mmrn2* (ref. 73) whereas lymphatic endothelial cells were enriched for *Lype1* (ref. 74) expression. All markers for each endothelial/epithelial SCL are listed in Supplementary Data 1.

Similar to findings in stroma/theca SCLs, one of the endothelial/epithelial SCLs was found to be enriched for GC markers and was removed from further analyses; no age differences were observed in this GC SCL. The only epithelial/endothelial SCL that showed age-related changes in the pathway analyses was the vascular endothelium; this SCL was found to have modestly increased DNA damage regulation (Fig. 8d). Another interesting observation was that upstream regulators of cellular senescence (TP53, CDKN1A and CDKN2A) were found to be increased with aging in vascular endothelial cells (Fig. 8e). Further analysis of genes downstream of TP53, CDKN1A and CDKN2A found these to be altered in directionality, consistent with the activation of these upstream regulators (Fig. 8f). This is consistent with studies indicating that vascular endothelial cells are highly susceptible to becoming senescent⁷⁵. In the ovary, cyclicity requires constant vascular remodeling⁶⁸, which we speculate may promote senescence in endothelial cells. However, despite observing increased TP53, CDKN1A and CDKN2A upstream regulator activity in the vascular endothelium SCL, the expression of *Cdkn1a* and *Cdkn2a* was unaffected by aging (Fig. 8g) whereas *Tp53* was not detected in our scRNA-seq analysis. Therefore, it remains unclear whether the vascular endothelium is a source of senescent cells in the aged ovary.

Discussion

In this report we assessed age-related changes in the mouse ovarian transcriptome at single-cell resolution. During aging, ovarian follicular reserve declines and there is a concomitant deterioration of the ovarian microenvironment as evidenced by increased inflammation and fibrosis. Importantly, these changes occur before follicular exhaustion¹¹ and probably contribute to decreased oocyte quality and diminished reproductive success until ovarian insufficiency occurs. However, specific cellular contributions to ovarian aging phenotypes are not yet elucidated, limiting the development of interventional approaches to extend female fertility. Whole-ovarian bulk transcriptomic assessments can provide results that are difficult to interpret due to potential changes in cell heterogeneity that occur during aging. Cell sorting can overcome this limitation but relies on specific antibodies or Cre-reporter systems to target specific cell types. scRNA-seq, on the other hand, is a useful tool for simultaneous measurement of transcriptomic changes in all ovarian cell types during the aging process. Previous ovarian scRNA-seq analyses have identified the molecular signatures of specific cell types and changes in individual cell populations^{18,26,28,59,76,77}.

In mice, estrous cycle²⁶ and primordial follicle assembly⁷⁶ result in dynamic changes in specific ovarian cellular populations. However, the specific cellular changes occurring during ovarian aging are still being elucidated, especially with regard to the critical period of diminished fertility that occurs long before follicular exhaustion. Because mice are the primary model organisms used for ovarian aging experiments²⁰, the single-cell ovarian aging atlas presented herein serves as a crucial resource for the field. In nonhuman primates, scRNA-seq has provided mechanistic insights into changes associated with ovarian aging¹⁸. However, this study was conducted with animals in the perimenopausal state⁷⁸ when alterations in cyclicity and hormone levels are perturbed. Our primary goal was to identify early changes that occur in reproductively aged mice before the periostropausal period. At 9 months of age mice experience declined ovarian reserve¹¹ but remain fertile⁷⁹, modeling a critical age when female humans seek to have children and experience difficulty conceiving². In humans a marked increase in embryonic aneuploidy is observed in embryos from donors, starting around 35 years of age⁸⁰, suggesting a loss in oocyte quality. With our approach, we differentiated all of the main cell types expected in the ovary and further subdivided them to determine specific cellular populations altered by the aging process.

Our scRNA-seq results show that the proportion of immune cells in the ovary doubles between 3 and 9 months of age. The most marked increase in immune cells within aged ovaries occurred in Types 1 and 17 lymphoid cells. A recent scRNA-seq assessment of ovarian immune cells reported an increase in CD4⁺CD8⁻ T cells, deemed double-negative T cells, in aged ovaries⁸¹. Many of the Types 1 and 17 lymphoid cells described in the present study, including $\alpha\beta$ DN, Type 17 NKTs, MAITs, $\gamma\delta$ Ts and a substantial proportion of Type 1 NKTs, are CD4⁺CD8⁻ and would therefore be included within the broad double-negative T cell population described in the previous study. Consistent with the previous report, our data indicate that many of these populations increase with age. However, our data provide better granularity and revealed changing in the aging ovary of specific populations of Types 1 and 17 lymphoid cells that had not previously been evaluated.

Specifically, we determined that the immune subpopulations that most consistently increased in the aged ovary were Type 1 NKTs and Type 17 $\gamma\delta$ Ts, both of which are innate T cells. Our data thus raise interesting questions about the functional roles of innate T lymphocytes in both the young and old ovary. Innate T cells are tissue-resident cells thought to contribute to the maintenance of tissue homeostasis and serve as sentinel cells in the detection of infectious agents, neoplastic cells or aberrant cellular damage⁸². In the female reproductive tract, innate lymphocytes show high functional diversity with both beneficial and detrimental effects⁸³. However, the role of innate lymphocytes in the ovary is an unexplored subject. Type 17 $\gamma\delta$ Ts play critical roles during fibrosis in a variety of organs, including liver^{84,85}, kidney⁸⁶, lung⁸⁷ and heart⁸⁸. However, whether these cells are protective or deleterious in fibrosis appears to be dependent on both tissue and context^{89,90}. For instance, age-related accumulation of Type 17 $\gamma\delta$ Ts contributes to chronic inflammation in adipose tissue⁹¹. In the ovary, expansion of Type 17 $\gamma\delta$ Ts could either promote fibrosis or be a compensatory attempt to dampen the fibrotic environment. Little is known about the role of Type 1 NKTs in the ovary. In general,

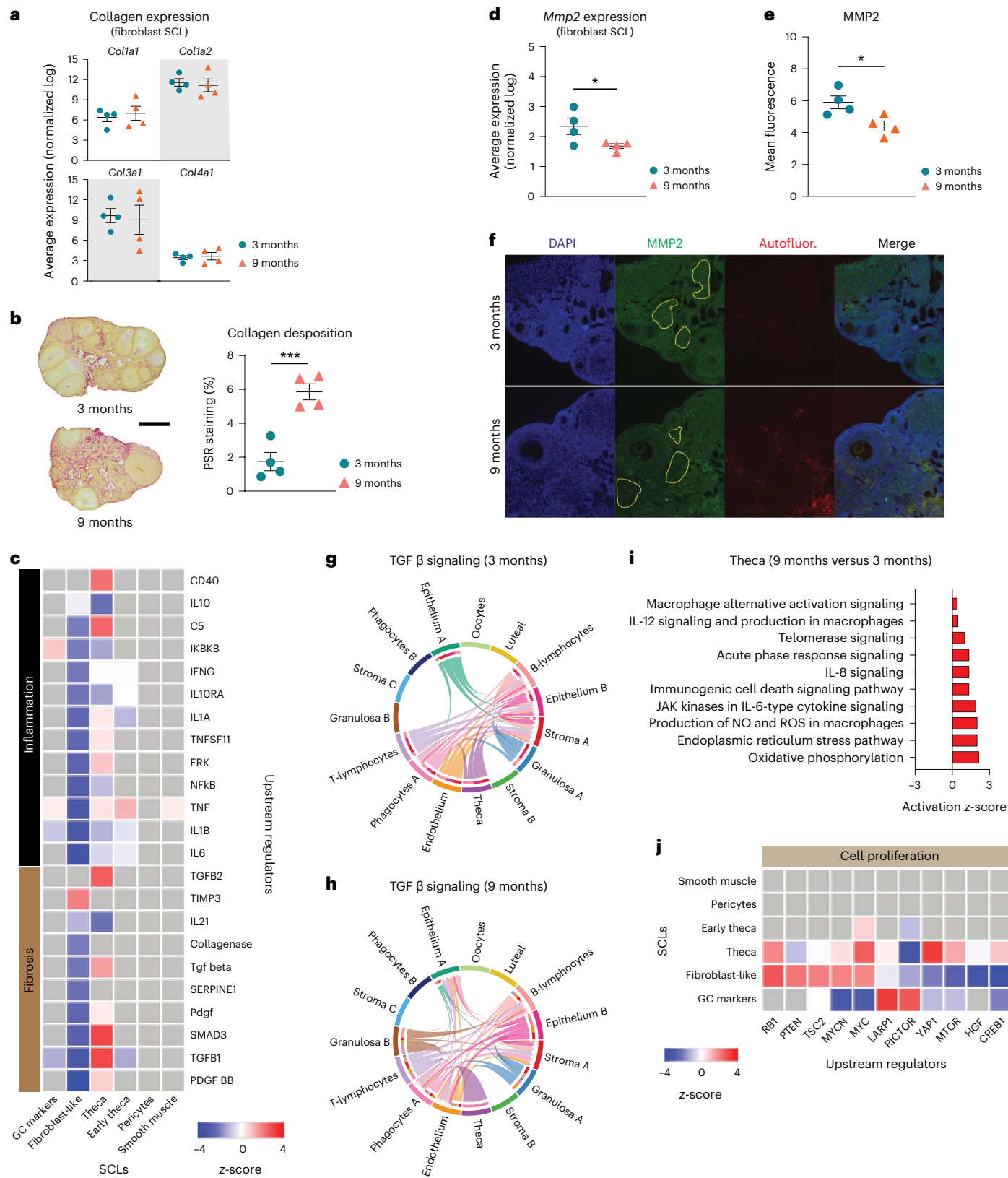
Fig. 6 | Biological significance of altered pathways in ovarian stroma and theca SCLs. **a**, Expression of collagen genes in the fibroblast-like stroma SCL does not change with age. **b**, Picrosirius red (PSR) staining of collagen deposition in 3- and 9-month-old ovaries. Scale bar, 500 μ m. **c**, IPA upstream regulator analyses of age-related changes in stroma and TC SCLs (9 versus 3 months old, z-score) related to inflammation and fibrosis. **d**, Expression of *Mmp2* gene in fibroblast-like stroma decreases with age. **e**, MMP2 protein is decreased in aged ovarian stroma, as shown by immunofluorescence. **f**, Representative immunofluorescence images of MMP2 (green), DAPI (blue) and autofluorescence (red). Yellow-bordered areas represent stromal regions analyzed, avoiding

follicles and autofluorescent regions. This assay was repeated independently for each biological replicate. **g, h**, CellChat chord diagrams of TGF β signaling pathway interactions in 3-month (**g**) and 9-month ovarian CLUs (**h**). **i**, IPA canonical pathways indicating activation of specific pathways by aging in TCs. **j**, IPA upstream regulator analyses of age-related changes in stroma and TC SCLs (9 versus 3 months old, z-score) related to cell proliferation ($n = 5$ per age group). scRNA-seq was performed in $n = 4$ ovaries per age group. Data presented as mean \pm s.e.m. *FDR < 0.05, **FDR = 0.01, ***FDR = 0.005 by one-tailed *t*-test (**a, b**) or two-tailed *t*-test (**d, e**). ROS, reactive oxygen species. Exact *P* values shown in Source Data.

NKTs provide important immune responses during injury, repair, inflammation and fibrosis in the liver and lung⁶⁷. Further mechanistic studies assessing the roles of these cells in ovarian fibrosis and inflammation are warranted.

Under normal conditions, tissue-resident lymphocytes are maintained through slow homeostatic proliferation⁹², as opposed

to adaptive T cells that are generally recruited from the circulation⁹³. The mechanisms underlying increased innate lymphocyte numbers in the aged ovary may be a result of increased proliferation in response to tissue remodeling and/or local inflammatory cytokine production. This hypothesis is consistent with increased IFNG, TNF, IL15 and IL1A upstream regulator activity in GC SCLs. Alternatively,



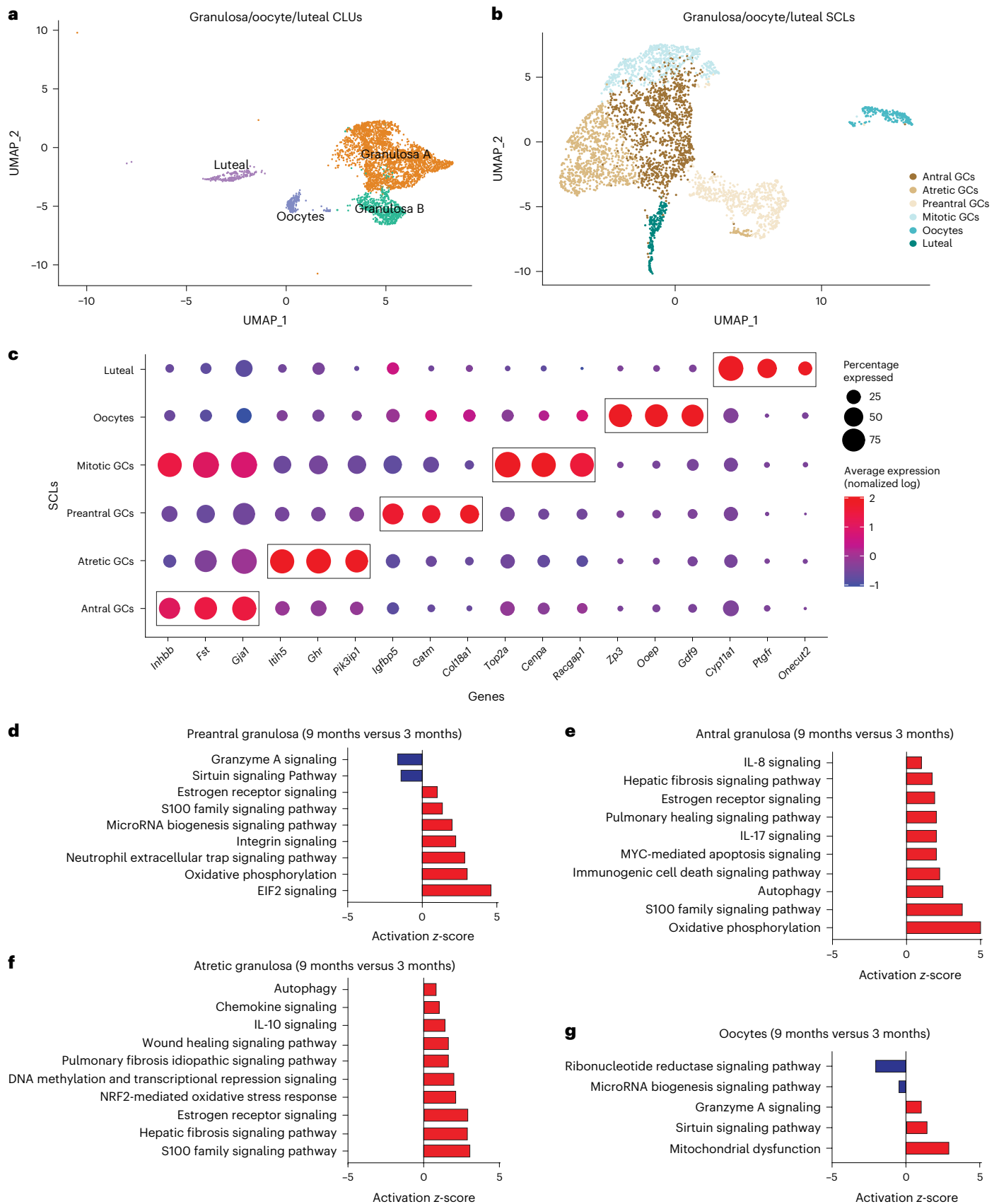


Fig. 7 | Subclustering of GCs, oocytes and luteal cells. **a**, UMAP of granulosa, oocyte and luteal cell CLUs used for subclustering. **b**, UMAP of granulosa, oocyte and luteal SCLs. **c**, Dot plot of markers used for SCL cell type identification.

d–g, Z-scores indicating activation or inhibition of pathways during aging by IPA analysis in preantral GCs (**d**), antral GCs (**e**), atretic GCs (**f**) and oocytes (**g**). scRNA-seq was performed in $n = 4$ ovaries per age group.

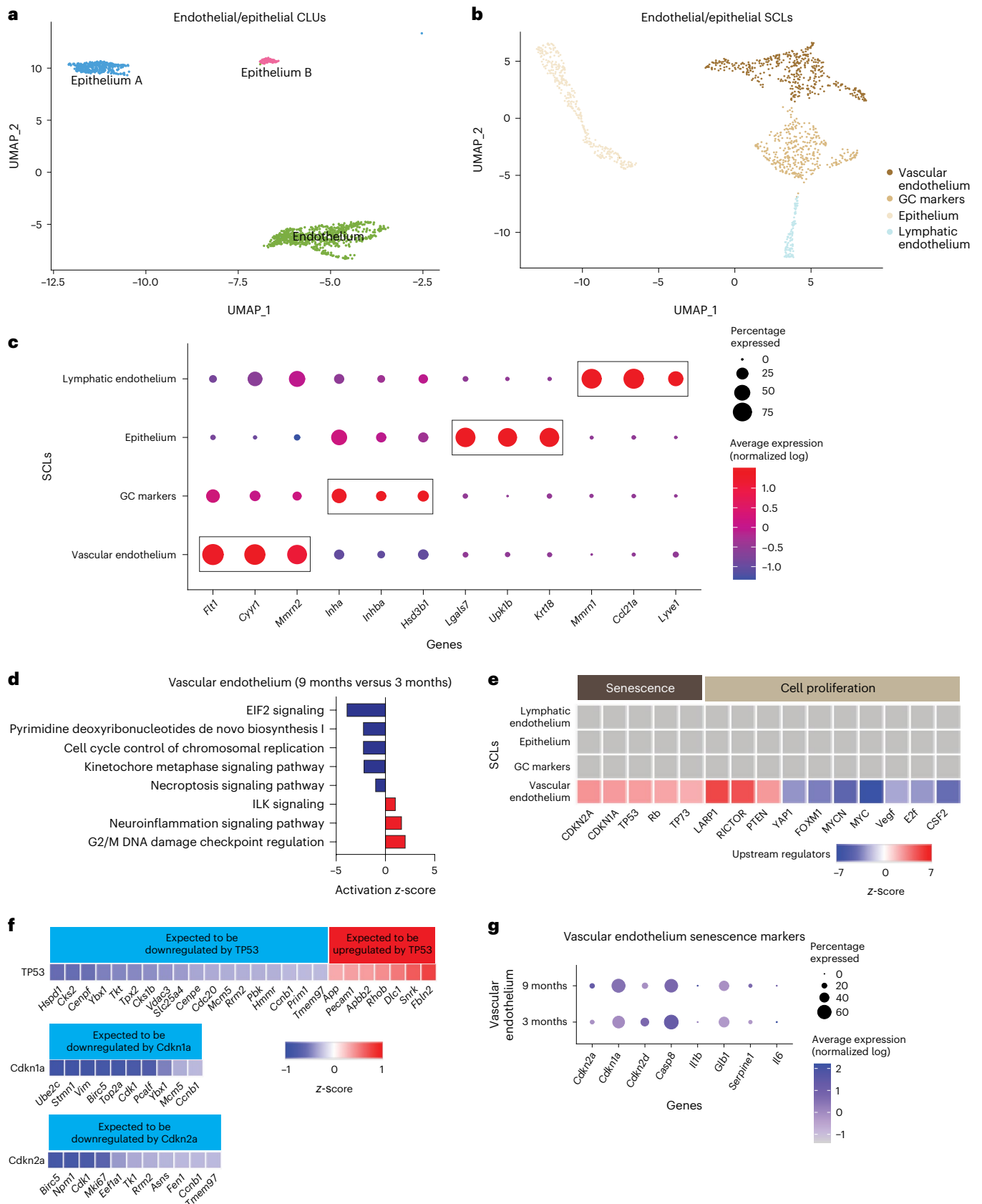


Fig. 8 | Subclustering of endothelial and epithelial cells. a, UMAP of endothelial and epithelial CLUs used for subclustering. **b**, UMAP of endothelial and epithelial SCLs. **c**, Dot plot of markers used for SCL cell type identification. **d**, Z-scores indicating activation or inhibition of pathways altered with aging, as evidenced by IPA analysis, in vascular endothelial cells. **e**, Z-scores indicating

activation or inhibition of upstream regulators during aging, as evidenced by IPA analysis, in endothelial and epithelial SCLs. **f**, Z-scores indicating up- or downregulation of genes by genes *TP53*, *Cdkn1a* and *Cdkn2a*. **g**, Dot plot showing expression of cell senescence markers in vascular endothelial cells in 3- and 9-month-old ovaries. scRNA-seq was performed in $n = 4$ ovaries per age group.

circulating lymphocytes could be recruited into tissue in response to similar proinflammatory signals⁹⁴. Chronic ovarian inflammation caused by autoimmune disease also promotes lymphocyte accumulation⁹⁵, and female humans with autoimmune diseases often experience ovarian insufficiency⁹⁶. This suggests an association between the accumulation of lymphocytes and age-related follicular declines, which merits future interrogation.

Although we detected an increase in the proportion of B cells within the scRNA-seq data at 9 months of age, this was not confirmed by flow cytometry. A previous report showed that the proportion of ovarian B cells slightly increased from 2 to 6 months of age but then returned to basal levels by 12 months of age¹³. This suggests that B cell numbers are highly variable in the aging ovary. Within our scRNA-seq data we also detected an increase in CD4⁺ T cells in the 9-month-old ovary. Although the proportion of CD4⁺ T cells decreased between 3 and 9 months of age according to flow cytometry, the absolute number of these cells increased with age. The accumulation of CD4⁺ T cells was previously reported in the aged ovary¹³, although these changes were not observed until 12 months of age. This suggests that the accumulation of CD4⁺ T cells may begin to occur at 9 months of age.

The literature addressing age-related changes in ovarian myeloid cells is conflicting^{13,81,97}, which may be due to differences in the methods employed and ages evaluated. We found no significant changes in ovarian myeloid cell accumulation by 9 months of age through scRNA-seq or flow cytometry analyses. At this juncture it remains unclear whether myeloid cells actually increase in the ovary with advancing age, but the fusion of monocytes and macrophages into MNGCs⁹⁸ could confound these interpretations. As addressed previously, MNGC accumulation is a hallmark of the aged ovary⁴⁹. Previous reports suggest that MNGCs may contribute to the age-related deterioration of the ovarian microenvironment¹⁷. However, the mechanisms that promote MNGC formation and their physiological ramifications in the ovary remain unresolved. The best-characterized MNGCs are osteoclasts, which are implicated in bone remodeling through phagocytosis of apoptotic cells and collagen fragments⁹⁹. In the ovary, MNGCs may also serve similar functions because phagocytic processes control tissue remodeling during follicular atresia, corpora lutea regression and ovulation. Interestingly, because estrogen induces osteoclast apoptosis, menopausal-related loss of estrogen action accelerates bone loss in humans¹⁰⁰. Similarly, decreased estrogen signaling in the aged ovary may promote MNGC accumulation. Lymphocytes, which are increased in the aged ovary, also contribute to MNGC formation through cytokine-mediated mechanisms¹⁰¹. For example, IL17a (the primary cytokine produced by Type 17 lymphoid cells) is associated with osteoclast formation¹⁰², which suggests that Type 17 lymphoid cells may contribute to MNGC formation in the aged ovary. Similarly, IFNG is known to induce MNGC formation^{103,104}. Our data show that the primary source of *Ifng* production in the ovary is Type 1 lymphoid cells, which accumulate in the ovary during aging. Additional studies will be required to further elucidate the mechanisms underlying MNGC formation in the ovary and the role they play in ovarian function and aging processes.

The aforementioned accumulation of lymphoid cells and MNGCs almost certainly contributes to pathological changes that occur in the aged ovary. We speculate that they crosstalk with follicular cells to induce immunogenic responses that adversely affect the local microenvironment. For instance, GCs show upregulated IL-17 and IFNG pathway activity with advancing age, although these genes are dominantly expressed in lymphocytes. This supports the notion that lymphoid cells produce proinflammatory ligands that alter GC transcriptional networks. We also found that GCs upregulate oxidative stress pathways, which we surmise may occur in response to the proinflammatory environment. This finding is supported by a scRNA-seq analysis of aged nonhuman primate ovaries that also show declines in oxidoreductase pathway activity in GCs¹⁸. These similarities were observed despite the

nonhuman primate ovaries being collected during the perimenopausal period, whereas the mouse ovaries were collected before the peri-estropausal period. In addition to immunogenic responses, we also found that GCs and TCs display age-related induction of fibrotic responses as evidenced by increased TGF β pathway activation. In alignment with previous observations^{12,14,15}, we saw increased ovarian collagen deposition by 9 months of age. Because collagen is primarily produced by stromal fibroblast-like cells^{14,105}, we evaluated the expression of collagen genes in this SCL but found no age-related changes. Conversely, the collagenase pathway and MMP2 expression were downregulated in the stroma of aged ovaries, suggesting that collagen accumulation occurs due to declines in degradation. It is also noteworthy that TCs upregulate cell proliferation pathways (for example, mTOR), which increase with aging¹⁰⁶ but, more importantly, have been linked to the activation of primordial follicles¹⁰⁷.

Although the data presented herein serve as an important tool for hypothesis generation, there are a few limitations that should be noted. Cell preparation for scRNA-seq and flow cytometry requires filtration steps that remove MNGCs and large oocytes from analyses. Future studies employing laser-capture microscopy and single-nuclei sequencing would allow for interrogation of these large-cellular populations. Even though the mouse is the most common model organism used for ovarian assessment, there are important aspects of their ovarian biology that differ from nonhuman primates and humans: for example, humans are a mono-ovulating species whereas mice are polyovulating and therefore follicular selection signaling probably differs between these species. In addition, virgin mice were used in this study, which does not account for the impact of pregnancy on ovarian aging dynamics. The examination of additional time points following reproductive senescence should also be considered, because it would provide critical insights related to how the ovary changes following the loss of fertility, which may impact systemic aging mechanisms. Finally, estropause in mice does not completely recapitulate the changes observed in nonhuman primate and human menopause. As such, other models of ovarian aging should be evaluated before definitive conclusions are drawn.

In summary, this report provides insight into changes that occur within the aging murine ovary at single-cell resolution. We report that, by 9 months of age, when mice remain fertile and reproductively active, immune cell accumulation is already doubled with the greatest changes being observed in innate lymphocytes including Type 1 NKTs and Type 17 $\gamma\delta$ Ts. We also demonstrate that GCs and TCs upregulate stress-response, immunogenic and fibrotic signaling pathways with aging. These changes correspond to declines in collagenase expression in the stroma, which we surmise contributes to collagen accumulation with age. These changes were accompanied by accumulation of MNGCs with advancing age, which accounted for the vast majority of lipofuscin positivity in aged ovaries. This observation, coupled with the increase in immune cells that commonly express transcriptional markers of cellular senescence, probably contributes to the previously reported increase in ovarian cellular senescence with advancing age. Collectively, our findings provide insights into the underlying mechanisms that promote chronic ovarian inflammation and fibrosis with advancing age and serve as an important resource for the field.

Methods

Animals and tissue collection and dissociation for scRNA-seq

All animal procedures were approved by the Institutional Animal Care and Use Committee at the Oklahoma Medical Research Foundation. C57BL/6J (strain no. 000664) female mice ($n = 8$) were purchased from the Jackson Laboratory and acclimated to the Oklahoma Medical Research Foundation animal facility before ovary collection. During acclimation, mice were maintained at $22 \pm 0.5^\circ\text{C}$ on a 12/12-h light/dark cycle and had ad libitum access to food (LabDiet no. 5053, Purina) and water. At 3 ($n = 4$) or 9 months of age ($n = 4$), mice were anesthetized with isoflurane and euthanized by exsanguination via cardiac

puncture. Perfusion was performed with $1\times$ PBS, and ovaries collected and dissected. One ovary from each mouse was dissociated using Multi Tissue Dissociation Kit 1 (cat. no. 130110201, Miltenyi Biotec), following the manufacturer's instructions, to create a single-cell suspension in Dulbecco's PBS (cat. no. 14287080, Gibco).

scRNA-seq library construction

scRNA-seq libraries were constructed with the Chromium Single Cell 3' GEM, Library & Gel Bead Kit v.3 (cat. no. 10000075, 10X Genomics), according to the manufacturer's instructions, as briefly described below. Following the creation of ovarian single-cell suspensions, cells were counted on a MACSQuant10 flow cytometer and diluted to $1,000\text{ cells }\mu\text{l}^{-1}$ to target the recovery of 5,000 cells per sample during scRNA-seq encapsulation. The diluted cells, master mix, gel beads and partitioning oil were added to the Chromium Single Cell B Chip (cat. no. 10000073, 10X Genomics) and loaded into a Chromium controller (cat. no. 1000204, 10X Genomics) to generate the gel beads-in-emulsion (GEMs) for downstream library preparation. GEMs were then transferred to PCR strip tubes and incubated in a thermocycler to perform reverse transcription in GEMs. Following reverse transcription in GEMs, the recovery agent was aspirated and complementary DNA was cleaned using the Dynabeads MyOne SILANE reagent included in the scRNA-seq kit. The cDNA was amplified and then cleaned using SPRISelect reagent beads (cat. no. B23318, Beckman Coulter). The cDNA was quality checked using a High Sensitivity D5000 ScreenTape (cat. no. 5067-5592, Agilent) run on a TapeStation 2200 (cat. no. G2964AA, Agilent). An aliquot of 25% of amplified cDNA was carried forward to library preparation. Libraries were quantified by quantitative PCR and quality checked on a High Sensitivity D1000 ScreenTape (cat. no. 5067-5584, Agilent) on the TapeStation 2220. Libraries were normalized, pooled and sequenced on a NovaSeq6000 PE150 flow cell. The sequence depth obtained was $\sim 50,000$ reads per cell.

scRNA-seq quality control and data analysis

Fastq files were generated and demultiplexed from raw base call (bcl) files using the cellranger mkfastq pipeline. Alignment, filtering, barcode counting and unique molecular identifier counting were conducted with the cellranger count pipeline using the refdata-gex-mm10-2020-A reference transcriptome with default settings. The resultant out files were loaded into R Studio (v.4.2.2) using the 'load10X' function of the SoupX package¹⁰⁸. The SoupX pipeline was then used to estimate and remove ambient RNA contamination before conversion to Seurat objects¹⁰⁹. Samples were then merged to create a single Seurat object and filtered based on the number of features (>200) and percentage mitochondrial transcripts ($<25\%$). Genes expressed in fewer than three cells were removed from analysis. Genes representing ribosomal contamination (*Malat1*, *Gm42418*, *Gm26917*, *Ay036118*)^{110,111} were causing technical background noises and were thus removed from the analysis to improve subclustering. Variable features were identified in Seurat before scaling data and running principal component analysis. The JackStraw method was used to determine the dimensionality of the dataset, and UMAP analysis was generated in Seurat. Doublets were identified and removed using the DoubletFinder package¹¹², with 5% doublets expected. Other parameters ($pN=0.25$, $pK=0.01$) were generated using DoubletFinder sweep statistics. Samples were coprojected on a UMAP that was used to determine that there were no batch effects and that further data integration was not necessary. Seurat was used to find differentially expressed genes by CLU and age and to generate plots presented in the figures (that is, DimPlot, VlnPlot and DotPlot). Module scores were calculated by the average expression levels of each program at single-cell level, subtracted by the aggregated expression of control feature sets. To assess cell-to-cell interactions between different ovarian cell types in young and aged mouse ovaries we used CellChat45 (v.1.6.1), which is based on the expression of known ligand-receptor pairs¹¹³. Gene lists were imported into IPA 01.12 (Qiagen

Bioinformatics) software to assess pathway/biological function enrichment analysis.

Histology

The remaining ovary from each mouse was collected into 4% paraformaldehyde, processed and serially sectioned. To determine ovarian reserve, one of every six serial sections from the whole ovary was hematoxylin and eosin (H&E) stained and follicles from each state were counted as described previously¹¹⁴. The number of preantral follicles (primordial, primary and secondary) was multiplied by six to account for sections that were not evaluated and then multiplied by two to account for both ovaries. Due to their large size, antral follicles were multiplied by three to account for sections that were not evaluated and then multiplied by two to account for both ovaries. Picrosirius red staining for collagen deposition and Sudan black staining for lipofuscin accumulation were performed on one randomly assigned section from the midline of each ovary and analyzed as previously described^{11,12}.

Immunofluorescence

Evaluation of MMP2 protein in the ovarian stroma was performed in paraffin-embedded ovarian sections as previously described¹¹⁵. Slides were incubated with primary rabbit anti-MMP2 antibody (1:100; cat. no. 87809, BioLegend) overnight, followed by secondary goat anti-rabbit IgG Alexa Fluor 488 antibody (1:500; cat. no. 2338052, Jackson ImmunoResearch Laboratories) for 1 h and DAPI for 5 min. Images were captured on a Zeiss fluorescent microscope in the green (MMP2) and blue (DAPI) channels. Images were also taken in the red channel to identify and avoid autofluorescent regions in the ovary, which are common in the aged ovary⁴³. The mean fluorescent intensity from three MMP2-stained stromal regions from each mouse was quantified by ImageJ and averaged. Nonspecific background fluorescence was calculated in a similar manner using secondary-only stained serial sections from the same mouse. The nonspecific signal was subtracted from each sample.

Flow cytometry

High-parameter spectral flow cytometry was performed to confirm age-related changes in the percentage and number of immune cells. C57BL/6J (strain no. 000664) female mice ($n = 30$) were purchased from the Jackson Laboratory. To obtain sufficient cells for the gating strategy proposed, six ovaries from three mice were pooled ($n = 5$ per age group). Before euthanasia, vaginal cytology was performed to determine estrous cycle stage as previously described⁹². The mice were anesthetized with isoflurane and intravenously injected with $2\text{ }\mu\text{g}$ of FITC-anti-CD45 mAb (cat. no. 35-0454, Cytex) to label intravascular cells and distinguish them from tissue-resident extravascular leukocytes¹¹⁶. Five minutes after labeling, mice were euthanized and ovaries collected and pooled according to estrous cycle stage. Ovarian cells were isolated by enzymatic digestion in 3 ml of DMEM (cat. no. D6429, Sigma) containing 4 mg of collagenase (cat. no. C5138-100MG, Sigma-Aldrich). Samples were incubated at $37\text{ }^\circ\text{C}$ for 40 min and gently pipetted 30 times every 10 min to encourage tissue dissociation⁹³. Following dissociation, cells were passed through a $70\text{-}\mu\text{m}$ filter (cat. no. 130-098-462, Miltenyi Biotec) and washed with an additional 7 ml of DMEM. Cells were labeled with Zombie NIR (cat. no. 423106, BioLegend) according to the manufacturer's instructions then washed in FACS Buffer (PBS + 5% newborn calf serum), incubated with a Fc blocking reagent (anti-mouse CD16/32, cat. no. 70-0161, Cytex), washed and stained with a surface-staining, fluorochrome-labeled mAb cocktail (Supplementary Data 1) for 30 min at $4\text{ }^\circ\text{C}$, in the presence of Brilliant Stain Buffer Plus ($10\text{ }\mu\text{l}$ per sample; cat. no. 563795, Becton Dickinson) and CellBlox Blocking Buffer ($5\text{ }\mu\text{l}$ per sample; cat. no. C001T02F01, Thermo Fisher Scientific). Cells were washed again in FACS buffer and intracellularly stained to detect transcription factor expression using the True-Nuclear Transcription Factor Buffer Set (cat. no. 424401,

BioLegend) according to the manufacturer's instructions. At the end of the procedure, stained cells were fixed in 2% paraformaldehyde for 5 min. Stained cells were acquired using a five-laser Cytek Aurora flow cytometer and analyzed using FlowJo 10.9 (Becton Dickinson). The gating strategy can be seen in Supplementary Fig. 4.

Statistics and reproducibility

Differentially expressed genes between CLUs and by age were called in the Seurat package using the FindMarkers command with default parameters. Differentially expressed gene lists were imported into IPA software and filtered on false discovery rate (FDR) < 0.1 and log(fold change) > 0.25 for pathway analyses. Pathways with $P < 0.05$ were considered statistically significant, and activation z-scores are reported by heatmap or bar charts in the figures. More traditional statistical analyses were performed using GraphPad Prism software. The Shapiro–Wilk test was performed to confirm normal distribution of data. Strip plots are presented with individual points shown and means \pm s.e.m. indicated. For comparison of means between the two ages, Student's *t*-tests were used, applying one- and two-tailed tests where appropriate¹⁷. Corrections for multiple comparisons were made, where appropriate, using the Benjamini, Krieger and Yekutieli correction for multiple comparisons. Significant differences were defined at $P < 0.05$ or FDR < 0.05 (for multiple comparisons). No statistical methods were used to determine the number of biological replicates to use. Our sample size was selected based on sample sizes reported in previous similar publications^{18,81}. Because the experimental groups used in this study were separated by age, it was not possible to randomize samples. No samples were removed from analysis. All criteria for data exclusion were pre-established. Cells with >400 unique molecular identifier counts, >200 genes or >25% of mitochondrial RNA counts were filtered. Also, cells expressing contradictory markers of known different cell types were removed as potential doublets. One of the cell CLUs was present in only one sample and presented oviduct cell markers rather than ovarian cell markers; this CLU was considered as oviduct tissue contamination and was removed from further analysis. Histological assessments were performed in a blinded manner. For single-cell library preparation, the sample order was randomized and the person preparing the samples blinded to sample grouping. For single-cell data analysis, blinding was not possible due to the statistical methods chosen for comparison by group. Each sample was given assigned group-identifying metadata. Identities have to be called during coding to assess differential expression between groups. It is not possible to perform the correct analysis without knowing from which group each identity is determined. All samples were treated equivalently during quality control steps.

Reporting summary

Further information on research design is available in the Nature Portfolio Reporting Summary linked to this article.

Data availability

The datasets generated through this work are available in a publicly accessible repository. Raw and processed data files can be downloaded from NCBI Gene Expression Omnibus at accession no. [GSE232309](https://www.ncbi.nlm.nih.gov/geo/query/acc.cgi?acc=GSE232309). An interactive Shiny-based web application is also available at <https://omrf.shinyapps.io/OvarianAgingSCAtlas/>. Sequencing data for the study of Morris et al.²⁶ were retrieved from Open Science Framework and the Broad Institute Single Cell Portal under study no. SCP1914. Gene lists are available as Supplementary Data files. Source Data are provided with this paper.

Code availability

The scRNA-seq data analysis was performed using scripts in R, which are available in GitHub: OvarianAgingAtlas (github.com/StoutLab/OvarianAgingAtlas).

References

- Johnson, J. A. & Tough, S. No-271-delayed child-bearing. *J. Obstet. Gynaecol. Can.* **39**, e500–e515 (2017).
- Broekmans, F. J., Soules, M. R. & Fauser, B. C. Ovarian aging: mechanisms and clinical consequences. *Endocr. Rev.* **30**, 465–493 (2009).
- Levine, M. E. et al. Menopause accelerates biological aging. *Proc. Natl Acad. Sci. USA* **113**, 9327–9332 (2016).
- Wellons, M., Ouyang, P., Schreiner, P. J., Herrington, D. M. & Vaidya, D. Early menopause predicts future coronary heart disease and stroke: the Multi-Ethnic Study of Atherosclerosis. *Menopause* **19**, 1081–1087 (2012).
- Tchernof, A., Calles-Escandon, J., Sites, C. K. & Poehlman, E. T. Menopause, central body fatness, and insulin resistance: effects of hormone-replacement therapy. *Coron. Artery Dis.* **9**, 503–511 (1998).
- Muka, T. et al. Association of age at onset of menopause and time since onset of menopause with cardiovascular outcomes, intermediate vascular traits, and all-cause mortality: a systematic review and meta-analysis. *JAMA Cardiol.* **1**, 767–776 (2016).
- Ossewaarde, M. E. et al. Age at menopause, cause-specific mortality and total life expectancy. *Epidemiology* **16**, 556–562 (2005).
- May-Panloup, P. et al. Ovarian ageing: the role of mitochondria in oocytes and follicles. *Hum. Reprod. Update* **22**, 725–743 (2016).
- Lim, J. & Luderer, U. Oxidative damage increases and antioxidant gene expression decreases with aging in the mouse ovary. *Biol. Reprod.* **84**, 775–782 (2011).
- Yang, L. et al. The role of oxidative stress and natural antioxidants in ovarian aging. *Front. Pharmacol.* **11**, 617843 (2020).
- Ansere, V. A. et al. Cellular hallmarks of aging emerge in the ovary prior to primordial follicle depletion. *Mech. Ageing Dev.* **194**, 111425 (2021).
- Briley, S. M. et al. Reproductive age-associated fibrosis in the stroma of the mammalian ovary. *Reproduction* **152**, 245–260 (2016).
- Lliberos, C. et al. Evaluation of inflammation and follicle depletion during ovarian ageing in mice. *Sci. Rep.* **11**, 278 (2021).
- Amargant, F. et al. Ovarian stiffness increases with age in the mammalian ovary and depends on collagen and hyaluronan matrices. *Ageing Cell* **19**, e13259 (2020).
- Umehara, T. et al. Female reproductive life span is extended by targeted removal of fibrotic collagen from the mouse ovary. *Sci. Adv.* **8**, eabn4564 (2022).
- Mara, J. N. et al. Ovulation and ovarian wound healing are impaired with advanced reproductive age. *Ageing (Albany NY)* **12**, 9686–9713 (2020).
- Foley, K. G., Pritchard, M. T. & Duncan, F. E. Macrophage-derived multinucleated giant cells: hallmarks of the aging ovary. *Reproduction* **161**, V5–V9 (2021).
- Wang, S. et al. Single-cell transcriptomic atlas of primate ovarian aging. *Cell* **180**, 585–600 (2020).
- Wang, S. et al. Spatiotemporal analysis of human ovarian aging at single-cell resolution. Preprint at *Research Square* <https://doi.org/10.21203/rs.3.rs-1624864/v1> (2022).
- Lu, H. et al. Current animal model systems for ovarian aging research. *Ageing Dis.* **13**, 1183–1195 (2022).
- Russ, J. E., Haywood, M. E., Lane, S. L., Schoolcraft, W. B. & Katz-Jaffe, M. G. Spatially resolved transcriptomic profiling of ovarian aging in mice. *iScience* **25**, 104819 (2022).
- Ankel-Simons, F. & Cummins, J. M. Misconceptions about mitochondria and mammalian fertilization: implications for theories on human evolution. *Proc. Natl Acad. Sci. USA* **93**, 13859–13863 (1996).

23. Zhang, D., Keilty, D., Zhang, Z. F. & Chian, R. C. Mitochondria in oocyte aging: current understanding. *Facts Views Vis. Obgyn* **9**, 29–38 (2017).
24. Zhang, G. et al. Expression of mitochondria-associated genes (PPARGC1A, NRF-1, BCL-2 and BAX) in follicular development and atresia of goat ovaries. *Reprod. Domest. Anim.* **50**, 465–473 (2015).
25. Muhl, L. et al. Single-cell analysis uncovers fibroblast heterogeneity and criteria for fibroblast and mural cell identification and discrimination. *Nat. Commun.* **11**, 3953 (2020).
26. Morris, M. E. et al. A single-cell atlas of the cycling murine ovary. *eLife* <https://doi.org/10.7554/eLife.77239> (2022).
27. Baek, S. H. et al. Single cell transcriptomic analysis reveals organ specific pericyte markers and identities. *Front. Cardiovasc. Med.* **9**, 876591 (2022).
28. Wagner, M. et al. Single-cell analysis of human ovarian cortex identifies distinct cell populations but no oogonial stem cells. *Nat. Commun.* **11**, 1147 (2020).
29. Marti, N. et al. Genes and proteins of the alternative steroid backdoor pathway for dihydrotestosterone synthesis are expressed in the human ovary and seem enhanced in the polycystic ovary syndrome. *Mol. Cell. Endocrinol.* **441**, 116–123 (2017).
30. Sontheimer, R. D., Racila, E. & Racila, D. M. C1q: its functions within the innate and adaptive immune responses and its role in lupus autoimmunity. *J. Invest. Dermatol.* **125**, 14–23 (2005).
31. Lin, G., Finger, E. & Gutierrez-Ramos, J. C. Expression of CD34 in endothelial cells, hematopoietic progenitors and nervous cells in fetal and adult mouse tissues. *Eur. J. Immunol.* **25**, 1508–1516 (1995).
32. Garcillan, B. et al. CD3G or CD3D knockdown in mature, but not immature, T lymphocytes similarly cripples the human TCRalpha complex. *Front. Cell Dev. Biol.* **9**, 608490 (2021).
33. Carpenter, A. R. et al. Uroplakin 1b is critical in urinary tract development and urothelial differentiation and homeostasis. *Kidney Int.* **89**, 612–624 (2016).
34. Berisha, B., Rodler, D., Schams, D., Sinowatz, F. & Pfaffl, M. W. Prostaglandins in superovulation induced bovine follicles during the preovulatory period and early corpus luteum. *Front. Endocrinol. (Lausanne)* **10**, 467 (2019).
35. Chu, P. G. & Arber, D. A. CD79: a review. *Appl. Immunohistochem. Mol. Morphol.* **9**, 97–106 (2001).
36. Hu, C. et al. CellMarker 2.0: an updated database of manually curated cell markers in human/mouse and web tools based on scRNA-seq data. *Nucleic Acids Res.* **51**, D870–D876 (2023).
37. Heng, T. S., Painter, M. W. & Immunological Genome Project, C. The Immunological Genome Project: networks of gene expression in immune cells. *Nat. Immunol.* **9**, 1091–1094 (2008).
38. Szabo, S. J. et al. A novel transcription factor, T-bet, directs Th1 lineage commitment. *Cell* **100**, 655–669 (2000).
39. Ivanov, I. I. et al. The orphan nuclear receptor RORgammat directs the differentiation program of proinflammatory IL-17⁺ T helper cells. *Cell* **126**, 1121–1133 (2006).
40. Savage, A. K. et al. The transcription factor PLZF directs the effector program of the NKT cell lineage. *Immunity* **29**, 391–403 (2008).
41. Kovalovsky, D. et al. The BTB-zinc finger transcriptional regulator PLZF controls the development of invariant natural killer T cell effector functions. *Nat. Immunol.* **9**, 1055–1064 (2008).
42. Coletta, S. et al. The immune receptor CD300e negatively regulates T cell activation by impairing the STAT1-dependent antigen presentation. *Sci. Rep.* **10**, 16501 (2020).
43. Asano, Y. Age-related accumulation of non-heme ferric and ferrous iron in mouse ovarian stroma visualized by sensitive non-heme iron histochemistry. *J. Histochem. Cytochem.* **60**, 229–242 (2012).
44. Urzua, U., Chacon, C., Espinoza, R., Martinez, S. & Hernandez, N. Parity-dependent hemosiderin and lipofuscin accumulation in the reproductively aged mouse ovary. *Anal. Cell Pathol. (Amst.)* **2018**, 1289103 (2018).
45. Evangelou, K. & Gorgoulis, V. G. Sudan Black B, the specific histochemical stain for lipofuscin: a novel method to detect senescent cells. *Methods Mol. Biol.* **1534**, 111–119 (2017).
46. Ruan, J. et al. Novel Myh11 dual reporter mouse model provides definitive labeling and identification of smooth muscle cells—brief report. *Arterioscler. Thromb. Vasc. Biol.* **41**, 815–821 (2021).
47. Deaton, R. A. et al. A new autosomal Myh11-CreER(T2) smooth muscle cell lineage tracing and gene knockout mouse model—brief report. *Arterioscler. Thromb. Vasc. Biol.* **43**, 203–211 (2023).
48. Rosas-Canyelles, E., Dai, T., Li, S. & Herr, A. E. Mouse-to-mouse variation in maturation heterogeneity of smooth muscle cells. *Lab Chip* **18**, 1875–1883 (2018).
49. Martinez, F. O., Helming, L. & Gordon, S. Alternative activation of macrophages: an immunologic functional perspective. *Annu. Rev. Immunol.* **27**, 451–483 (2009).
50. Steiger, S. et al. Immunomodulatory molecule IRAK-M balances macrophage polarization and determines macrophage responses during renal fibrosis. *J. Immunol.* **199**, 1440–1452 (2017).
51. Li, Y. L., Sato, M., Kojima, N., Miura, M. & Senoo, H. Regulatory role of extracellular matrix components in expression of matrix metalloproteinases in cultured hepatic stellate cells. *Cell Struct. Funct.* **24**, 255–261 (1999).
52. Nelson, J. F., Felicio, L. S., Randall, P. K., Sims, C. & Finch, C. E. A longitudinal study of estrous cyclicity in aging C57BL/6J mice: I. Cycle frequency, length and vaginal cytology. *Biol. Reprod.* **27**, 327–339 (1982).
53. Davidson, S. et al. Fibroblasts as immune regulators in infection, inflammation and cancer. *Nat. Rev. Immunol.* **21**, 704–717 (2021).
54. Knight, P. G. & Glister, C. TGF-beta superfamily members and ovarian follicle development. *Reproduction* **132**, 191–206 (2006).
55. McCloskey, C. W. et al. Metformin abrogates age-associated ovarian fibrosis. *Clin. Cancer Res.* **26**, 632–642 (2020).
56. Li, M. O., Wan, Y. Y., Sanjabi, S., Robertson, A. K. & Flavell, R. A. Transforming growth factor-beta regulation of immune responses. *Annu. Rev. Immunol.* **24**, 99–146 (2006).
57. Dompe, C. et al. Human granulosa cells—stemness properties, molecular cross-talk and follicular angiogenesis. *Cells* <https://doi.org/10.3390/cells10061396> (2021).
58. Meinsohn, M. C. et al. Single-cell sequencing reveals suppressive transcriptional programs regulated by MIS/AMH in neonatal ovaries. *Proc. Natl Acad. Sci. USA* <https://doi.org/10.1073/pnas.2100920118> (2021).
59. Fan, X. et al. Single-cell reconstruction of follicular remodeling in the human adult ovary. *Nat. Commun.* **10**, 3164 (2019).
60. Chen, A. Q., Wang, Z. G., Xu, Z. R., Yu, S. D. & Yang, Z. G. Analysis of gene expression in granulosa cells of ovine antral growing follicles using suppressive subtractive hybridization. *Anim. Reprod. Sci.* **115**, 39–48 (2009).
61. Wigglesworth, K., Lee, K. B., Emori, C., Sugiura, K. & Eppig, J. J. Transcriptomic diversification of developing cumulus and mural granulosa cells in mouse ovarian follicles. *Biol. Reprod.* **92**, 23 (2015).
62. Lee, J. H. & Berger, J. M. Cell cycle-dependent control and roles of DNA topoisomerase II. *Genes (Basel)* <https://doi.org/10.3390/genes10110859> (2019).
63. Blanchard, J. M. Cyclin A2 transcriptional regulation: modulation of cell cycle control at the G1/S transition by peripheral cues. *Biochem. Pharmacol.* **60**, 1179–1184 (2000).
64. Piersanti, R. L., Santos, J. E. P., Sheldon, I. M. & Bromfield, J. J. Lipopolysaccharide and tumor necrosis factor-alpha alter gene expression of oocytes and cumulus cells during bovine in vitro maturation. *Mol. Reprod. Dev.* **86**, 1909–1920 (2019).

65. Stocco, C., Telleria, C. & Gibori, G. The molecular control of corpus luteum formation, function, and regression. *Endocr. Rev.* **28**, 117–149 (2007).
66. Salmon, N. A., Handyside, A. H. & Joyce, I. M. Oocyte regulation of anti-Mullerian hormone expression in granulosa cells during ovarian follicle development in mice. *Dev. Biol.* **266**, 201–208 (2004).
67. Shrikhande, L., Shrikhande, B. & Shrikhande, A. AMH and its clinical implications. *J. Obstet. Gynaecol. India* **70**, 337–341 (2020).
68. Brown, H. M. & Russell, D. L. Blood and lymphatic vasculature in the ovary: development, function and disease. *Hum. Reprod. Update* **20**, 29–39 (2014).
69. Brown, H. M., Robker, R. L. & Russell, D. L. Development and hormonal regulation of the ovarian lymphatic vasculature. *Endocrinology* **151**, 5446–5455 (2010).
70. Hartanti, M. D. et al. Formation of the bovine ovarian surface epithelium during fetal development. *J. Histochem. Cytochem.* **68**, 113–126 (2020).
71. Hummitzsch, K. et al. A new model of development of the mammalian ovary and follicles. *PLoS ONE* **8**, e55578 (2013).
72. Schulz, A. et al. The soluble Fms-like tyrosine kinase-1 contributes to structural and functional changes in endothelial cells in chronic kidney disease. *Int. J. Mol. Sci.* <https://doi.org/10.3390/ijms232416059> (2022).
73. Galvagni, F. et al. Dissecting the CD93-Multimerin 2 interaction involved in cell adhesion and migration of the activated endothelium. *Matrix Biol.* **64**, 112–127 (2017).
74. Fujimoto, N. et al. Single-cell mapping reveals new markers and functions of lymphatic endothelial cells in lymph nodes. *PLoS Biol.* **18**, e3000704 (2020).
75. Bloom, S. I., Islam, M. T., Lesniewski, L. A. & Donato, A. J. Mechanisms and consequences of endothelial cell senescence. *Nat. Rev. Cardiol.* **20**, 38–51 (2023).
76. Wang, J. J. et al. Single-cell transcriptome landscape of ovarian cells during primordial follicle assembly in mice. *PLoS Biol.* **18**, e3001025 (2020).
77. Pei, J. et al. Single-cell transcriptomics analysis reveals a cell atlas and cell communication in yak ovary. *Int. J. Mol. Sci.* <https://doi.org/10.3390/ijms24031839> (2023).
78. Gilardi, K. V., Shideler, S. E., Valverde, C. R., Roberts, J. A. & Lasley, B. L. Characterization of the onset of menopause in the rhesus macaque. *Biol. Reprod.* **57**, 335–340 (1997).
79. Isola, J. V. V. et al. Mild calorie restriction, but not 17 α -estradiol, extends ovarian reserve and fertility in female mice. *Exp. Gerontol.* **159**, 111669 (2022).
80. Frasiak, J. M. et al. The nature of aneuploidy with increasing age of the female partner: a review of 15,169 consecutive trophectoderm biopsies evaluated with comprehensive chromosomal screening. *Fertil. Steril.* **101**, 656–663 e651 (2014).
81. Ben Yaakov, T., Wasserman, T., Akin, E. & Savir, Y. Single-cell analysis of the aged ovarian immune system reveals a shift towards adaptive immunity and attenuated cell function. *eLife* <https://doi.org/10.7554/eLife.74915> (2023).
82. Masopust, D. & Soerens, A. G. Tissue-resident T cells and other resident leukocytes. *Annu. Rev. Immunol.* **37**, 521–546 (2019).
83. Yuzen, D., Arck, P. C. & Thiele, K. Tissue-resident immunity in the female and male reproductive tract. *Semin. Immunopathol.* **44**, 785–799 (2022).
84. Wang, X. & Tian, Z. Gammadelta T cells in liver diseases. *Front. Med.* **12**, 262–268 (2018).
85. Hammerich, L. et al. Chemokine receptor CCR6-dependent accumulation of gammadelta T cells in injured liver restricts hepatic inflammation and fibrosis. *Hepatology* **59**, 630–642 (2014).
86. Peng, X. et al. IL-17A produced by both gammadelta T and Th17 cells promotes renal fibrosis via RANTES-mediated leukocyte infiltration after renal obstruction. *J. Pathol.* **235**, 79–89 (2015).
87. Simonian, P. L. et al. Gammadelta T cells protect against lung fibrosis via IL-22. *J. Exp. Med.* **207**, 2239–2253 (2010).
88. Yan, X. et al. Deleterious effect of the IL-23/IL-17A axis and gammadelta T cells on left ventricular remodeling after myocardial infarction. *J. Am. Heart Assoc.* **1**, e004408 (2012).
89. Bank, I. The role of $\gamma\delta$ T cells in fibrotic diseases. *Rambam Maimonides Med. J.* <https://doi.org/10.5041/RMMJ.10256> (2016).
90. Zhang, M. & Zhang, S. T cells in fibrosis and fibrotic diseases. *Front. Immunol.* **11**, 1142 (2020).
91. Bruno, M. E. C. et al. Accumulation of gammadelta T cells in visceral fat with aging promotes chronic inflammation. *Geroscience* **44**, 1761–1778 (2022).
92. Moutouou, M. M., Gauthier, S. D., Chen, N., Leboeuf, D. & Guimond, M. Studying peripheral T cell homeostasis in mice: a concise technical review. *Methods Mol. Biol.* **2111**, 267–283 (2020).
93. Nguyen, Q. P., Deng, T. Z., Witherden, D. A. & Goldrath, A. W. Origins of CD4^(hi) circulating and tissue-resident memory T-cells. *Immunology* **157**, 3–12 (2019).
94. Wilkinson, P. C., Komai-Koma, M. & Newman, I. Locomotion and chemotaxis of lymphocytes. *Autoimmunity* **26**, 55–72 (1997).
95. Dong, Y. et al. The role of regulatory T cells in thymectomy-induced autoimmune ovarian disease. *Am. J. Reprod. Immunol.* <https://doi.org/10.1111/aji.12683> (2017).
96. Sharif, K. et al. Insights into the autoimmune aspect of premature ovarian insufficiency. *Best. Pract. Res. Clin. Endocrinol. Metab.* **33**, 101323 (2019).
97. Zhang, Z., Schlamp, F., Huang, L., Clark, H. & Brayboy, L. Inflammaging is associated with shifted macrophage ontogeny and polarization in the aging mouse ovary. *Reproduction* **159**, 325–337 (2020).
98. Ahmadzadeh, K., Vanoppen, M., Rose, C. D., Matthys, P. & Wouters, C. H. Multinucleated giant cells: current insights in phenotype, biological activities, and mechanism of formation. *Front. Cell Dev. Biol.* **10**, 873226 (2022).
99. Weivoda, M. M. & Bradley, E. W. Macrophages and bone remodeling. *J. Bone Miner. Res.* **38**, 359–369 (2023).
100. Kameda, T. et al. Estrogen inhibits bone resorption by directly inducing apoptosis of the bone-resorbing osteoclasts. *J. Exp. Med.* **186**, 489–495 (1997).
101. Goretzlehner, G., Krause, B., Nehmzow, M. & Ulrich, U. [Endocrine diseases in pregnancy]. *Z. Arztl. Fortbild. (Jena)* **84**, 135–141 (1990).
102. Adamopoulos, I. E. et al. IL-17A gene transfer induces bone loss and epidermal hyperplasia associated with psoriatic arthritis. *Ann. Rheum. Dis.* **74**, 1284–1292 (2015).
103. Anderson, J. M. Multinucleated giant cells. *Curr. Opin. Hematol.* **7**, 40–47 (2000).
104. Fais, S. et al. Multinucleated giant cells generation induced by interferon-gamma. Changes in the expression and distribution of the intercellular adhesion molecule-1 during macrophages fusion and multinucleated giant cell formation. *Lab. Invest.* **71**, 737–744 (1994).
105. Lind, A. K. et al. Collagens in the human ovary and their changes in the perifollicular stroma during ovulation. *Acta Obstet. Gynecol. Scand.* **85**, 1476–1484 (2006).
106. Liu, G. Y. & Sabatini, D. M. mTOR at the nexus of nutrition, growth, ageing and disease. *Nat. Rev. Mol. Cell Biol.* **21**, 183–203 (2020).
107. Schneider, A. et al. The interconnections between somatic and ovarian aging in murine models. *J. Gerontol. A Biol. Sci. Med. Sci.* **76**, 1579–1586 (2021).

108. Young, M. D. & Behjati, S. SoupX removes ambient RNA contamination from droplet-based single-cell RNA sequencing data. *Gigascience* <https://doi.org/10.1093/gigascience/giaa151> (2020).
109. Satija, R., Farrell, J. A., Gennert, D., Schier, A. F. & Regev, A. Spatial reconstruction of single-cell gene expression data. *Nat. Biotechnol.* **33**, 495–502 (2015).
110. Liu, Y. et al. Single-cell profiling reveals divergent, globally patterned immune responses in murine skin inflammation. *iScience* **23**, 101582 (2020).
111. Nguyen, H. T. T., Guevarra, R. B., Magez, S. & Radwanska, M. Single-cell transcriptome profiling and the use of AID deficient mice reveal that B cell activation combined with antibody class switch recombination and somatic hypermutation do not benefit the control of experimental trypanosomiasis. *PLoS Pathog.* **17**, e1010026 (2021).
112. McGinnis, C. S., Murrow, L. M. & Gartner, Z. J. DoubletFinder: doublet detection in single-cell RNA sequencing data using artificial nearest neighbors. *Cell Syst.* **8**, 329–337 (2019).
113. Jin, S. et al. Inference and analysis of cell-cell communication using CellChat. *Nat. Commun.* **12**, 1088 (2021).
114. Isola, J. V. V. et al. 17Alpha-estradiol promotes ovarian aging in growth hormone receptor knockout mice, but not wild-type littermates. *Exp. Gerontol.* **129**, 110769 (2020).
115. Saccon, T. D. et al. Primordial follicle reserve, DNA damage and macrophage infiltration in the ovaries of the long-living Ames dwarf mice. *Exp. Gerontol.* **132**, 110851 (2020).
116. Anderson, K. G. et al. Intravascular staining for discrimination of vascular and tissue leukocytes. *Nat. Protoc.* **9**, 209–222 (2014).
117. Ruxton, G. D. & Neuhäuser, M. When should we use one-tailed hypothesis testing? *Methods Ecol. Evol.* <https://doi.org/10.1111/j.2041-210X.2010.00014.x> (2010).

Acknowledgements

This work was supported by the National Institutes of Health (nos. R01 AG069742 to M.B.S. and P30 AG050911 to W.M.F.), the Global Consortium for Reproductive Longevity and Equality (nos. GCRLE-4501 to M.B.S and GCRLE-0523 to S.R.O.) and the Presbyterian Health Foundation (Pilot Research Funding to M.B.S.). The funders had no role in study design, data collection and analysis, decision to publish or preparation of the manuscript. We thank the staff at the Clinical Genomics Center, Flow Cytometry Core (Cytek Aurora, grant no. 1S10OD028479-01) and Imaging Core Facility at the Oklahoma Medical Research Foundation for assistance with sequencing and histological procedures.

Author contributions

J.V.V.I., S.R.O. and M.B.S. conceived the project and designed the experiments. J.V.V.I. and S.R.O. performed the experiments and data analyses, with contributions from C.R.H., S.K., S.A.M., J.D.H., H.N.C.C., A.S., S.K., J.A.-I. and W.M.F. J.V.V.I., S.R.O. and C.R.H. created figures and performed statistical analyses, with contributions from W.M.F. and M.B.S. J.V.V.I., S.R.O. and M.B.S. wrote the manuscript, and all authors edited and approved the final draft.

Competing interests

The authors declare no competing interests.

Additional information

Supplementary information The online version contains supplementary material available at <https://doi.org/10.1038/s43587-023-00552-5>.

Correspondence and requests for materials should be addressed to Michael B. Stout.

Peer review information *Nature Aging* thanks the anonymous reviewer(s) for their contribution to the peer review of this work.

Reprints and permissions information is available at www.nature.com/reprints.

Publisher's note Springer Nature remains neutral with regard to jurisdictional claims in published maps and institutional affiliations.

Open Access This article is licensed under a Creative Commons Attribution 4.0 International License, which permits use, sharing, adaptation, distribution and reproduction in any medium or format, as long as you give appropriate credit to the original author(s) and the source, provide a link to the Creative Commons license, and indicate if changes were made. The images or other third party material in this article are included in the article's Creative Commons license, unless indicated otherwise in a credit line to the material. If material is not included in the article's Creative Commons license and your intended use is not permitted by statutory regulation or exceeds the permitted use, you will need to obtain permission directly from the copyright holder. To view a copy of this license, visit <http://creativecommons.org/licenses/by/4.0/>.

© The Author(s) 2024

Reporting Summary

Nature Portfolio wishes to improve the reproducibility of the work that we publish. This form provides structure for consistency and transparency in reporting. For further information on Nature Portfolio policies, see our [Editorial Policies](#) and the [Editorial Policy Checklist](#).

Statistics

For all statistical analyses, confirm that the following items are present in the figure legend, table legend, main text, or Methods section.

n/a Confirmed

- The exact sample size (n) for each experimental group/condition, given as a discrete number and unit of measurement
- A statement on whether measurements were taken from distinct samples or whether the same sample was measured repeatedly
- The statistical test(s) used AND whether they are one- or two-sided
Only common tests should be described solely by name; describe more complex techniques in the Methods section.
- A description of all covariates tested
- A description of any assumptions or corrections, such as tests of normality and adjustment for multiple comparisons
- A full description of the statistical parameters including central tendency (e.g. means) or other basic estimates (e.g. regression coefficient) AND variation (e.g. standard deviation) or associated estimates of uncertainty (e.g. confidence intervals)
- For null hypothesis testing, the test statistic (e.g. F , t , r) with confidence intervals, effect sizes, degrees of freedom and P value noted
Give P values as exact values whenever suitable.
- For Bayesian analysis, information on the choice of priors and Markov chain Monte Carlo settings
- For hierarchical and complex designs, identification of the appropriate level for tests and full reporting of outcomes
- Estimates of effect sizes (e.g. Cohen's d , Pearson's r), indicating how they were calculated

Our web collection on [statistics for biologists](#) contains articles on many of the points above.

Software and code

Policy information about [availability of computer code](#)

Data collection NovaSeq 6000 System used to generate sequencing data.

Data analysis Generated sequencing data was analyzed using QIAGEN Ingenuity Pathway Analysis (<https://digitalinsights.qiagen.com/products-overview/discovery-insights-portfolio/analysis-and-visualization/qiagen-ipa/>), RStudio (<http://www.rstudio.com/>, version 4.2.2), SoupX (<https://github.com/constantAmateur/SoupX>), Cell Ranger (<https://support.10xgenomics.com/single-cell-gene-expression/software/overview/welcome>, version 3.1), Seurat (<https://github.com/satijalab/seurat>, version 4.3.0), SeuratWrappers (<https://github.com/satijalab/seurat-wrappers>, version 0.3.1), DoubletFinder (<https://github.com/chris-mcginnis-ucsf/DoubletFinder>, version 2.0.3), scCustomize (<https://github.com/samuel-marsh/scCustomize>, version 1.1.1), ShinyCell (<https://github.com/SGDDNB/ShinyCell>, version 2.1.0), CellChat (<https://github.com/sqjin/CellChat>, version 1.6.1). In-house scripts can be accessed at <https://github.com/StoutLab/OvarianAgingAtlas>.

For manuscripts utilizing custom algorithms or software that are central to the research but not yet described in published literature, software must be made available to editors and reviewers. We strongly encourage code deposition in a community repository (e.g. GitHub). See the Nature Portfolio [guidelines for submitting code & software](#) for further information.

Data

Policy information about [availability of data](#)

All manuscripts must include a [data availability statement](#). This statement should provide the following information, where applicable:

- Accession codes, unique identifiers, or web links for publicly available datasets
- A description of any restrictions on data availability
- For clinical datasets or third party data, please ensure that the statement adheres to our [policy](#)

The datasets generated through this work are available in a publicly accessible repository. Raw and processed data files can be downloaded from NCBI Gene Expression Omnibus at accession number GSE232309. An interactive Shiny-based web application is also available at <https://omrf.shinyapps.io/OvarianAgingSCAtlas/>. Sequencing data for the Morris et al. (2022) study were retrieved from Open Science Framework and the Broad Institute Single Cell Portal under study number SCP1914. Gene lists are available as supplementary data files and data underlying dot plots is available as source data files.

Research involving human participants, their data, or biological material

Policy information about studies with [human participants or human data](#). See also policy information about [sex, gender \(identity/presentation\), and sexual orientation](#) and [race, ethnicity and racism](#).

Reporting on sex and gender	NA
Reporting on race, ethnicity, or other socially relevant groupings	NA
Population characteristics	NA
Recruitment	NA
Ethics oversight	NA

Note that full information on the approval of the study protocol must also be provided in the manuscript.

Field-specific reporting

Please select the one below that is the best fit for your research. If you are not sure, read the appropriate sections before making your selection.

- Life sciences Behavioural & social sciences Ecological, evolutionary & environmental sciences

For a reference copy of the document with all sections, see nature.com/documents/nr-reporting-summary-flat.pdf

Life sciences study design

All studies must disclose on these points even when the disclosure is negative.

Sample size	For scRNA-Seq, n=4 biological replicates/group were sequenced with ~2000 cells/sample. No statistical methods were used to determine the number of biological replicates to use. Our sample size was selected based on sample sizes reported in previous similar publications (PMID: 32004457, 33351795, 33378681, 37096871). Additionally, we used SCOPIT Power calculations to determine that ~12,000 cells were needed to observe >100 cells per cluster, assuming that the rarest population was 1% of the total cells. Thus, we targeted 16,000 cells to ensure enough cells were available to make conclusions about rare populations.
Data exclusions	No samples were removed from analysis. All criteria for data exclusion were pre-established. Cells with less than 400 UMI counts, less than 200 genes, or greater than 25% of mitochondrial RNA counts were filtered. Also, cells expressing contradictory markers of known different cell types were removed as potential doublets. One of the cell clusters was present in only one sample and presented oviduct cell markers rather than ovarian cell markers. This cluster was considered oviduct tissue contamination and removed from further analysis.
Replication	Four biological replicates were included for each group. All biological replicates were successful and included in analysis. Single-cell findings were verified by orthogonal methods where possible, including flow cytometry and histological assessments. Findings were compared and integrated with previously published datasets.
Randomization	Since the experimental groups used in this study were separated by age, it was not possible to randomize samples. Mice were purchased from the Jackson Laboratory at the intended ages.
Blinding	Histological assessments were performed in a blinded manner. For single-cell library preparation, the sample order was randomized and the person preparing the samples were blinded to the sample grouping. For single-cell data analysis, blinding was not possible due to the statistical methods chosen to compare by group. Each sample was given assigned group-identifying meta-data. The identities have to be called during coding in order to assess differential expression between groups. It is not possible to perform the correct analysis without knowing from which group each identity is from. All samples were treated equivalently during quality control steps.

Reporting for specific materials, systems and methods

We require information from authors about some types of materials, experimental systems and methods used in many studies. Here, indicate whether each material, system or method listed is relevant to your study. If you are not sure if a list item applies to your research, read the appropriate section before selecting a response.

Materials & experimental systems

- n/a Involved in the study
- Antibodies
- Eukaryotic cell lines
- Palaeontology and archaeology
- Animals and other organisms
- Clinical data
- Dual use research of concern
- Plants

Methods

- n/a Involved in the study
- ChIP-seq
- Flow cytometry
- MRI-based neuroimaging

Antibodies

Antibodies used

Flow cytometry
 CD45.2 FITC 104 1 mg/ml Cytex Biosciences (Cat. No. 35-0454)
 CD90 BUV395 53-2.1 1/100 BD Biosciences (Cat. No. 740205)
 CD4 BUV563 GK1.5 1/400 BD Biosciences (Cat. No. 612923)
 CD69 BUV737 H1.2F3 1/200 BD Biosciences (Cat. No. 612793)
 MRI-5-OP-R1J-TFT RV421 - 1/400 NIH Tetramer Facilities
 Ly-6G BV510 1A8 1/100 Biolegend (Cat. No. 127633)
 CD44 BV650 IM7 1/100 Biolegend (Cat. No. 103049)
 CD103 BV711 M290 1/100 BD Biosciences (Cat. No. 564320)
 TCRgd BV786 GL3 1/100 BD Biosciences (Cat. No. 740995)
 CD19 RB545 103 1/100 BD Biosciences (Cat. No. 569727)
 CD11b NFB610-30S M1/70 1/100 Thermo Fisher Scientific (Invitrogen) (Cat. No. M015T02B05)
 CD8a PerCP-Cy5.5 53-6. 7 1/100 Biolegend (Cat. No. 100734)
 CD1d-PBS-57-TET PE - 1/800 NIH Tetramer Core Facility
 B220 PE-F700 RA3-6B2 1/100 Biolegend (Cat. No. 103280)
 TCRb PE-Cy7 H57-597 1/100 Biolegend (Cat. No. 109222)
 CD49b APC DX5 1/100 Biolegend (Cat. No. 108910)
 MHC 11 AlexaFluor700 M5/114.15.2 1/200 Biolegend (Cat. No. 107622)
 CD45 APC Fire 810 30-FII 1/100 Biolegend (Cat. No. 103174)
 CellBlox Blocking Buffer 5 ul/test Thermo Fisher Scientific (Invitrogen) (Cat. No. B001T06F01)
 Brilliant Stain Buffer Plus 10 uL/test BD Biosciences (Cat. No. 566385)
 RORgt BV480 Q31-378 1/100 BD Biosciences (Cat. No. 567176)
 GATA-3 AF647 L50-823 1/100 BD Biosciences (Cat. No. 560068)
 T-bet PE/Dazzle 594 4B10 1/200 Biolegend (Cat. No. 644828)

Immunofluorescence
 MMP-2 (D2O4T) Rabbit mAb 1/100 Cell Signaling (Cat. No. 87809)
 IgG Alexa Fluor 488 antibody 1/500 Jackson ImmunoResearch Laboratories (Cat. No. 2338052)

Validation

The CD1d and MR1 tetramers are not commercially available. They were obtained from the NIH Tetramer Core Facility (<https://tetramer.yerkes.emory.edu/>) and validated on normal mouse tissues using negative control tetramers supplied by the same facility. All other antibodies used were commercially available and previously validated in mice for the application used, as stated in the manufacturers websites: <https://wwwbdbiosciences.com>, <https://www.biolegend.com/en-gb>, <https://www.thermofisher.com/us/en/home/brands/invitrogen>, and <https://www.cellsignal.com>. Antibodies were also validated in-house under the staining conditions used.

Animals and other research organisms

Policy information about [studies involving animals](#); [ARRIVE guidelines](#) recommended for reporting animal research, and [Sex and Gender in Research](#)

Laboratory animals

3- and 9-month-old C57Bl/6J female mice. Mice were kept at 22 ± 0.5°C on a 12:12-hour light-dark cycle and had ad libitum access to food and water.

Wild animals

No wild animals were used in the study.

Reporting on sex

Since this is an ovarian aging study we only evaluated female mice.

Field-collected samples

Ethics oversight

Note that full information on the approval of the study protocol must also be provided in the manuscript.

Flow Cytometry

Plots

Confirm that:

- The axis labels state the marker and fluorochrome used (e.g. CD4-FITC).
- The axis scales are clearly visible. Include numbers along axes only for bottom left plot of group (a 'group' is an analysis of identical markers).
- All plots are contour plots with outliers or pseudocolor plots.
- A numerical value for number of cells or percentage (with statistics) is provided.

Methodology

Sample preparation

Instrument

Software

Cell population abundance

Gating strategy

- Tick this box to confirm that a figure exemplifying the gating strategy is provided in the Supplementary Information.